Evaluating the Use of TROPICS Pathfinder Observations for Lunar Calibration

by

Juliana L. Chew

B.S., Massachusetts Institute of Technology (2022)

Submitted to the Department of Aeronautics and Astronautics
in partial fulfillment of the requirements for the degree of

Master of Science in Aeronautics and Astronautics

at the

MASSACHUSETTS INSTITUTE OF TECHNOLOGY

June 2023

Authored by: Juliana L. Chew
Department of Aeronautics and Astronautics
May 12, 2023

Certified by: Kerri Cahoy
Professor and Bisplinghoff Faculty Fellow
Thesis Supervisor

Accepted by: Jonathan P. How
R. C. Maclaurin Professor of Astronautics and Aeronautics
Chair, Graduate Program Committee

This page is intentionally left blank.

Evaluating the Use of TROPICS Pathfinder Observations for Lunar Calibration

by

Juliana L. Chew

Submitted to the Department of Aeronautics and Astronautics
on May 12, 2023, in partial fulfillment of the
requirements for the degree of
Master of Science in Aeronautics and Astronautics

ABSTRACT

Traditional two-point in-situ calibration systems for microwave radiometers use large, on-board hot targets [12]. Small satellites such as CubeSats, however, are unable to house these hot targets due to SWaP constraints. Instead, CubeSat radiometers such as the TROPICS Pathfinder use noise diodes as smaller alternative hot calibration targets [18]. Noise diodes can experience calibration drifts that must be characterized and accounted for to maintain the reliability of radiance measurements. Given the stability of lunar radiative transfer models in microwave frequencies, lunar vicarious calibration may be a feasible method to detect calibration drifts.

In this thesis, we evaluate the use of TROPICS Pathfinder observations for lunar calibration. We develop a lunar calibration approach that takes TROPICS observations as input, processes TROPICS data for lunar observations, estimates lunar intrusion temperature and scan geometry, and accounts for pointing error. We compare the lunar brightness temperature estimates and measured antenna temperatures to the lunar radiative transfer model developed by Yang and Burgdorf [21].

We test our lunar calibration model on TROPICS Pathfinder lunar observations from November and December 2021. Pathfinder's antenna temperatures are within 1 K and 2 K of the simulated antenna temperatures for the W/F and G bands, respectively. We find that even though the simulated antenna temperatures generally agree, work remains to improve agreement between measured and modeled lunar brightness temperatures. The antenna temperature differences can fluctuate by $\pm$2K, $\pm$4K, and $\pm$5K for the W, F, and G bands, respectively, so the reliability of this methods needs to be improved further before operational use for calibration. Possible ways to improve lunar calibration results include tuning Yang and Burgdorf's lunar model, additional pointing error analyses, and lunar calibration model adjustments.

Thesis Supervisor: Kerri Cahoy
Title: Professor and Bisplinghoff Faculty Fellow

Acknowledgments

Words cannot describe how grateful I am to have had Prof. Kerri Cahoy as an advisor since my sophomore year. Without her guidance and support over the past 4 years, I am not sure where I would be when figuring out my major and interests, let alone whether I wanted to continue with graduate school. Thank you so much for helping me find my way and for all the mentorship.

I would also like to thank Dr. William Blackwell, Dr. Martin Burgdorf, Dr. R. Vincent Leslie, Dr. Stephen Leroy, and Dr. Hu Yang for the feedback and advice on all TROPICS-related and lunar model related work. Their help when I was working with TROPICS data and the lunar model has been invaluable, and I have learned so much about calibration, satellites, and research.

In addition, I am thankful for the welcoming and supportive community in Prof. Cahoy's STAR Lab. This lab has truly been a place where I felt at home at MIT. I would like to extend my appreciation to my collaborators and friends in STAR Lab, including (but certainly not limited to): Mary Dahl for not only being my UROP supervisor for SPRINT but also my classmate and TA; Amelia Gagnon, Sammy Hasler, and Ilaria Petracca for their support and work in TROPICS ; Alex Meredith and Endrit Shehaj for their work with radio occultations; Joey Murphy for his lunar view simulation work; and Alex Meredith, Mary Dahl, and Christine Page for their efforts on our turtlebot demo. And, of course, thank you Mary Dahl, Maddie Garcia, Alex Meredith, Ilaria Petracca, and Sophia Vlahakis for creating an enjoyable, warm atmosphere in the cluster.

I can never forget the love and support from friends and family. To my friends remaining in Boston: Alex, Hannah, Lilian, Kat, Mindren, Paige, and Sohini, thank you for the weekly board game nights, check-ins, and dinner visits. To my mom, thank you for being there for me. I cannot describe how grateful I am for everything. Even though you are often on the other side of the country, you are always in my heart.

Contents

This page is intentionally left blank.

List of Figures

List of Tables

Chapter 1

Introduction

1.1 TROPICS Mission Science Goals

The Time Resolved Observations of Precipitation structure and storm Intensity with a Constellation of Smallsats (TROPICS) is an upcoming mission that was originally planned as a constellation of six, 3-U CubeSat microwave radiometers (MWRs). Due to a launch failure in 2022, it is now planned to consist of four, 3-U CubeSats instead. The reduced scale has now launched 2 of the 4 CubeSats in May 2023 and will provide 3-dimensional temperatures of tropical cyclones (TCs) with high spatial resolution and revisit times of at most 60 minutes [4].

As outlined in [4], the TROPICS mission's main science goals are to:

1. Determine the relationship between upper-level warm-core evolution, precipitation structure, and storm intensity changes,

2. Determine the relationship between environmental humidity fields and TC precipitation structure, and

3. Investigate how the more frequent microwave observations from TROPICS impact numerical and statistical intensity forecasts of TCs.

To fulfill these science goals, each TROPICS CubeSat will house a passive MWR that is able to measure 12 radio frequency channels spanning the W, F, and G bands.

Table 1.1 describes all TROPICS channels as well as their use.

Table 1.1: TROPICS Frequencies [4, 5]

Band	Channel	Frequency (GHz)	Purpose
W	1	91.65 +/- 1.4	Precipitation Measurement
F	2	114.5	Temperature Profile near Oxygen Absorption Line
	3	115.95	
	4	116.65	
	5	117.25	
	6	117.80	
	7	118.24	
	8	118.58	
G	9	184.41	Temperature Profile near Water Vapor Absorption Line
	10	186.51	
	11	190.31	
	12	204.80	Cloud Ice Measurements

To test the MWR instrument as well as the calibration and validation algorithms, the TROPICS engineering model CubeSat (called TROPICS Pathfinder) was launched in June 2021 as a precursor to the mission [18]. In this thesis, we evaluate Pathfinder observations for lunar calibration.

1.2 Microwave Radiometer Measurement Geometry

The TROPICS Pathfinder CubeSat is in a sun-synchronous Low Earth Orbit (LEO) with a period of approximately 97 minutes [19]. Table 1.2 displays Pathfinder's orbital parameters.

Table 1.2: Orbital Parameters of the TROPICS Pathfinder CubeSat [19]

Orbit Parameter	Value
Altitude (km)	528.8 - 544.2
Inclination (deg)	97.51
Longitude of the Ascending Node (deg)	330.29
Period (min)	97
NORAD ID	48901

The onboard microwave radiometer instrument scans at 30 RPM in the cross track (CT) direction. There are three main sampling sectors around the 360° rotation, as shown in Figure 1-1: the Earth Sector consisting of 81 samples, the Noise Diode Sector, and the Deep Space Sector. The latter two are the calibration sectors, each of which consist of 10 samples. Each sample represents approximately 1.5° of the revolution.

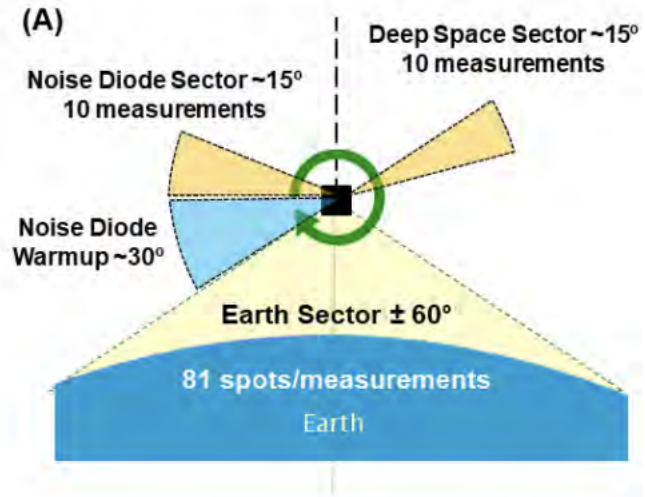

Figure 1-1: The TROPICS scan pattern. Each spot represents approximately 1.5° of each revolution [18].

1.3 Microwave Radiometer Calibration

MWRs typically use a 2-point calibration scheme when retrieving the radiance corresponding to a given digital count. These two points span the dynamic temperature range, with one "cold" and one "hot" point. A visualization of the 2-point calibration scheme is shown in Figure 1-2. For reliable measurements, TROPICS requires a calibration precision of at most 1 K or better [18].

To obtain measurements for the cold and hot calibration points, MWRs use a combination of onboard and vicarious targets. The selection of calibration targets is often based on physical constraints and the reliability of the models that estimate the targets' temperatures. Sections 1.3.1 and 1.3.2 describe popular calibration targets.

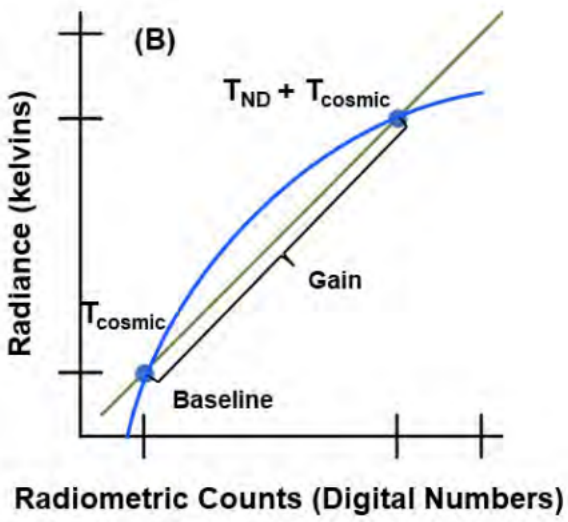

Figure 1-2: An example of the 2-point calibration scheme used for TROPICS. T_{cosmic} is the deep space temperature (or "cold" point), while $T_{ND} + T_{cosmic}$ refers to the combined noise diode and deep space measurement (the "hot" point). The "baseline" refers to the digital number (DN) corresponding to the "cold" point. The gain is the slope between these two calibration points, and the blue line accounts for the nonlinear term in the calibration algorithm. This nonlinear term is calculated using prelaunch calibration testing [18].

1.3.1 Onboard Calibration

Traditionally, onboard microwave calibration targets consist of bulky, conventional hot loads that act as RF blackbodies. Satellites such as the Global Precipitation Measurement (GPM) Microwave Imager (GMI) and the Meteorological Operational Satellite - Second Generation (MetOp-SG) use metal pyramids that are coated with RF-absorbing material as their hot loads [12, 20].

Recently, however, smaller calibration sources such as weakly coupled noise diodes have been on the rise because miniaturized satellites such as CubeSats are unable to house the legacy targets due to size, weight, and power (SWaP) constraints. The Jason Microwave Radiometer (JMR) launched in 2001 was the first mission to use noise diode calibration, and GMI uses a dual calibration system consisting of both traditional onboard hot loads and noise diodes [6, 11]. The TROPICS CubeSats, including Pathfinder, also use noise diodes for calibration [18].

Although better suited for miniaturized satellites, noise diodes require additional

testing and monitoring due to their unstable power output [18]. Brown et al. found that noise diode behavior is not only unpredictable but also unique to each individual component [7]. While some noise diodes aboard the JMR were stable over the first 4 years of operation, others' effective temperatures drifted between 0.2% and 3% [6]. Similarly, most noise diodes aboard the GMI stabilized within 4 years, but the 10 GHz noise diode continued to fluctuate in temperature [10]. Given that the effective noise diode temperature (denoted as T_{ND} in Figure 1-2) plays a key role in calibration, these drifts can affect the calculated antenna temperatures and later radiances. Brown et al. demonstrated that continuous calibration drift monitoring and recalibration can correct these effects and improve instrument accuracy and reliability [7].

1.3.2 Vicarious Calibration

Vicarious calibration refers to the use of external resources such as Earth's surface, deep space, and the Moon for calibration. In this section, we outline how each resource is used.

The Earth's surface is often used to calibrate both cold and warm scenes. Calm ocean measurements are used for cold scene calibration, with drier atmospheres being preferred to reduce frequency-dependent atmospheric interference [6, 23]. In addition, forests are used for vicarious warm scene calibration. Dense forest canopies (particularly that of the Amazon forest) can be approximated as a blackbody due to their depolarizing effects and their emissivity's predictable dependence with frequency [7, 23]. Radiative transfer models that simulate forest brightness temperatures have been developed by Brown and Ruf as well as Yang et al., with the former focusing on the Amazon forest and the latter extending the approach to boreal and temperate forests [23]. Yang et al. was able to detect 0.1 K calibration anomalies in the GMI using their radiative transfer model [23].

Deep space is typically used as the cold point in calibration because its brightness temperature is stable and unique for microwave frequencies. Microwave sounders such as TROPICS Pathfinder model the deep space temperature using the Rayleigh-Jeans approximation (or some variant), so the temperatures are thus considered known

quantities [18]. The deep space temperatures used in TROPICS Pathfinder's calibration are shown in Table 1.3.

Table 1.3: Deep Space Temperatures for the TROPICS Pathfinder Frequency Channels

Channel	**Deep Space Temperature (K)**
1	6.4819
2	4.5461
3	4.5614
4	4.5689
5	4.5753
6	4.5812
7	4.5860
8	4.5897
9	5.4622
10	5.4948
11	5.5544
12	5.7894

During these deep space scans, however, the Moon can pass into the antenna field of view (FOV) in an event called a lunar intrusion. If left unchecked, the Moon's higher brightness temperature can "contaminate" deep space readings and thus affect the two-point calibration scheme.

To account for these lunar intrusions, these "contaminated" deep space measurements are detected and often either corrected for or excluded from calibration. For instance, Yang and Weng detect lunar intrusions by thresholding the electronic boresight based on beamwidth [22]. They then correct these samples by comparing the contaminated sample measurements to clean deep-space views and modeling the increase in temperature due to the intrusion as function of antenna gain, lunar solid angle, and estimated lunar brightness temperature [22].

Rather than excluding or correcting for these "contaminated" samples, more recent efforts have focused on using lunar intrusions for vicarious calibration. Two main

avenues of research originate from this goal: (1), developing reliable lunar temperature models, and (2), formulating methods to compare lunar observations to said models.

Yang and Burgdorf validated a Lunar Microwave Radiative Transfer Model (RTM) previously developed by Keihm [16, 21]. Given the observational frequency and lunar phase as input, the RTM models the lunar temperature in a latitude-longitude grid formation on the Moon and then calculates the disk-averaged lunar brightness temperatures. The model accounts for the variation of lunar thermal properties given frequency and local time [21].

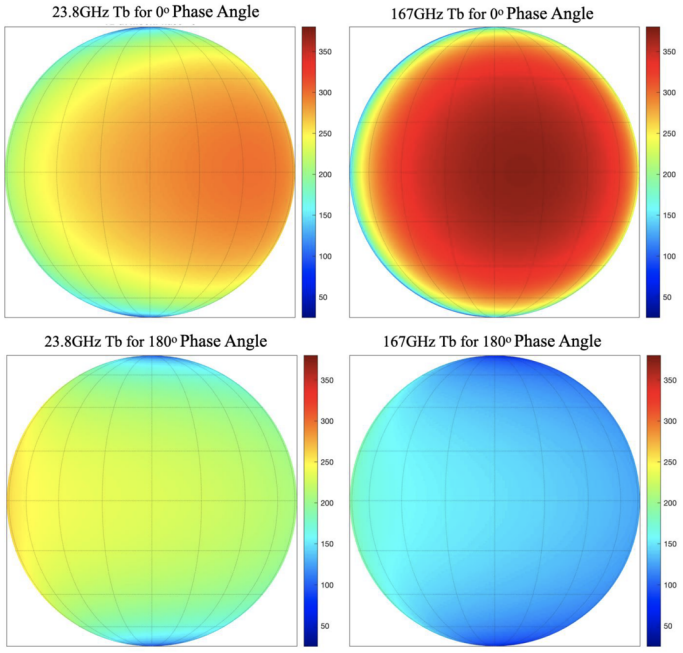

Figure 1-3: An example visualization of the RTM's lunar temperature grid for New Moon and Full Moon at 23.8 GHz and 167 GHz [21]. Here, 0° phase angle is Full Moon, and ±180° corresponds to New Moon.

To calibrate MWRs using Keihm's model, Yang and Burgdorf estimate the blackbody temperature of the Moon and then calculate the frequency-dependent lunar emissivities using lunar observations from the Advanced Technology Microwave Sounder (ATMS) [21]. They validate the calibrated model on lunar observations provided by Advanced Microwave Sounding Unit (AMSU) and the Microwave Humidity Sounder (MHS) onboard NOAA-16, 17, 18, 19, and Metop-A,B,C satellites for frequencies between 22 and 190 GHz. These lunar observations had the Moon pass through the

center of the antenna's FOV. As shown in Table 1.4, TROPICS has close frequency channel matchups to frequencies used in Tiger and Burgdorf's validation for channels 1 (91.65 GHz ± 1.4 GHz), 9 (183 GHz), and 11 (190.31 GHz).

Table 1.4: Approximate Matchups of TROPICS Pathfinder Frequency Channels and AMSU Frequency Channels used in Yang and Burgdorf's Validation [22]. For additional comparison, we include the bandwidths of the TROPICS Pathfinder and AMSU frequency channels from [1], [2], and [19] in the same order in which the instruments are listed.

TROPICS			**Matchup from [22]**		
Channel	**Frequency (GHz)**	**Bandwidth (MHz)**	**Frequency (GHz)**	**Bandwidth (MHz)**	**Instrument**
1	91.65 ± 1.4	1000	89	<6000, 1000, 2800	AMSU-A, AMSU-B, MHS
2	114.50	1000	None	None	None
3	115.95	800			
4	116.65	600			
5	117.25	600			
6	117.80	500			
7	118.24	380			
8	118.58	300			
9	184.41	2000	183	1000, 1000	AMSU-B, MHS
10	186.51	2000	None	None	None
11	190.31	2000	190	2200	MHS
12	204.80	2000	None	None	None

Yang and Burgdorf's validation demonstrates a mean error of less than 10 K in lunar brightness temperature [21]. They performed a sensitivity analysis to determine how errors in simulated lunar brightness temperature affect calculated antenna temperature accuracy when compared to MHS and AMSU measurements. Assuming accurate scan geometry and antenna beam characteristics, this lunar brightness temperature error corresponds to an antenna temperature error of 0.4 K in the W band for 2.2° beamwidth and 1 K in the G band for 1.1° beamwidth as shown in Figure 1-4 [21].

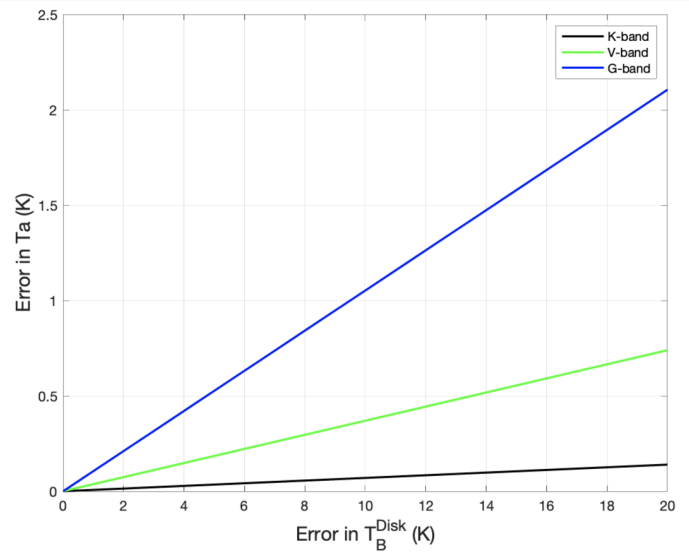

Figure 1-4: The relationship between the projected error in the disk-averaged lunar brightness temperature T_B^{Disk} and the corresponding antenna temperature Ta for the K, V/W, and G bands from Yang and Burgdorf's sensitivity analysis. The beamwidths are assumed to be 5.2°, 2.2°, and 1.1° for the K, V/W, and G bands, respectively. This error analysis demonstrates that the G band is more sensitive to errors in T_B^{Disk} [21].

Crews developed a lunar calibration algorithm based on sun-tracking ground radiometry methods [9]. This algorithm models measured antenna temperature as a function of the antenna scan geometry and the relative position and size of the Moon with respect to the antenna FOV center, where the FOV is the area spanning the antenna beamwidth. This algorithm was validated against ATMS lunar intrusion data, and the average residual was within the ATMS error budget of 0.6 K - 3.9 K [9].

In addition to developing a lunar calibration algorithm, Crews investigated the feasibility of lunar calibration for the TROPICS constellation. Their MATLAB simulations estimated that there are approximately 23, 19, and 11 lunar intrusions per one 96-minute TROPICS CubeSat orbit in the W, F, and G bands, respectively [9]. The frequency of lunar intrusions suggests that the Moon can potentially be used to track calibration drift over time.

1.4 Thesis Contributions

In this thesis, we develop a method for estimating lunar intrusion temperatures and electronic boresight angle measurements using TROPICS Pathfinder data. We also assess antenna pointing error using lunar intrusions and evaluate the feasibility of using TROPICS Pathfinder data for lunar calibration by comparing TROPICS lunar observations to Yang and Burgdorf's lunar simulation. We also assess the current lunar calibration model error and the feasibility of using TROPICS Pathfinder observations for lunar calibration. With this work, we create an initial framework for TROPICS lunar calibration that can be extended for future TROPICS CubeSats.

1.5 Thesis Organization

In Chapter 2, we outline the overall approach as well as the tools used for lunar calibration. From there, Chapter 3 details the data quality considerations and data preparation strategy for TROPICS lunar observations. In Chapter 4, we compare TROPICS observations to Yang and Burgdorf's RTM, characterize calibration error, and also analyze this method's sources of error. We then outline our conclusions and future work in Chapter 5, particularly possible extensions and improvements to the calibration method.

Chapter 2

Approach

Lunar calibration requires two sets of data: (1) on-orbit lunar observations made by the TROPICS radiometer, and (2) a lunar model; in this work, we use Yang and Burgdorf's modeled lunar data for comparison. In order to have a baseline for comparison in lunar calibration, we use simulated lunar data and treat it as truth as described in Section 2.1.

Before comparing the TROPICS Pathfinder measurements to Yang and Burgdorf's lunar model, we preprocess, align, and analyze the TROPICS on-orbit lunar observations. This chapter describes the datasets used in lunar calibration as well as the metrics used to assess the reliability and accuracy of the TROPICS Pathfinder lunar observations.

2.1 Lunar Model

We use Yang and Burgdorf's Lunar Radiative Transfer Model (RTM) for the simulation. This model is a Python tool that takes frequency and lunar phase as input and calculates the lunar temperature for lunar latitudes and longitudes [21]. From there, the model produces a look-up table of simulated disk-averaged lunar brightness temperatures.

Figure 2-1 displays the simulated disk-averaged lunar brightness temperatures as a function of lunar phase angle. Lunar phase angle is defined such that 0° is Full

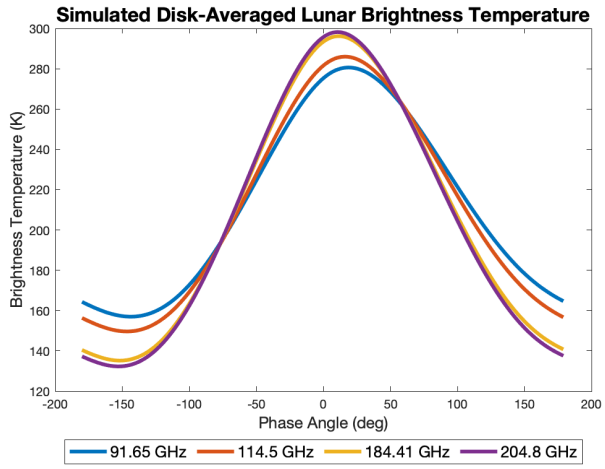

Figure 2-1: Disk-averaged lunar brightness temperatures outputted from Yang and Burgdorf's lunar RTM for selected TROPICS frequencies. From left to right in the legend, these frequencies correspond to Channel 1 (91.65 GHz), 2 (114.5 GHz), 9 (184.41 GHz), and 12 (204.8 GHz).

Moon and $\pm 180°$ is New Moon. As expected, lunar temperatures are at their lowest near New Moon and peak towards Full Moon. As a note, there is a phase offset between the simulated lunar brightness temperature and the lunar phase angle, so the simulated lunar brightness temperatures do not directly correspond to the lunar surface temperatures [21]. This behavior is expected because microwave frequencies penetrate the lunar surface at varying depths and due to parameters such as heat capacity, microwave absorption, and solar flux that depend on frequency, depth, and time [14]. We also expect to see the same behavior in Pathfinder's lunar observations.

In order to use Yang and Burgdorf's simulation for lunar calibration, we retrieve the time of the lunar intrusion as measured by TROPICS Pathfinder and find the corresponding lunar phase using ephemeris information provided by the Jet Propulsion Laboratory Horizons System [17]. From there, we use the lunar phase angle to look up the corresponding lunar temperature in Yang and Burgdorf's RTM.

In theory, lunar calibration should use the lunar phase angle as observed by TROPICS Pathfinder. However, we approximate this value by using the the lunar phase angle with respect to an Earth observer. TROPICS Pathfinder (and the future TROPICS CubeSats) are in LEO orbit, so this approximation will change the lunar phase

by at most 0.1°. Given that Yang and Burgdorf's RTM has a lunar phase resolution of 1°, this approximation has a negligible effect on lunar calibration.

2.2 TROPICS Data

We use the Level 1 data from the the TROPICS Data Processing Center (DPC), which contains the antenna temperature, calibration flags, and derived brightness temperatures. This dataset includes observations from October 2021 through January 2023.

The data fields are largely based on four main parameters representing the number of scans `n_scans`, the number of spots within the scan `n_spots`, the 12 channels, and the 10 cold calibration spots per scan. As each sample represents 1.5° of the scan, TROPICS can theoretically have 240 samples per scan. However, only areas designated to the calibration and Earth sectors are kept for analysis.

Table 2.1 displays the data fields, meanings, and dimensions for the data values used. Data fields related to pointing, particularly `encoderAngle_deg`, `moon_theta_F`, and `moon_theta_G`, are further described in Section 2.3.2.

Table 2.1: TROPICS Pathfinder Level 1 Data Fields Used in this Work

Field Name	**Meaning**	**Dimension**	**Units**
cC	Cold Calibration Digital Counts	10 x `n_scans` x 12	unitless
cC_CalFlag	Cold Calibration Outlier Flag	10 x `n_scans` x 12	unitless
intruLunarFlag	Binary Lunar Intrusion Flag	240 x `n_scans` x 12	unitless
intruSolarFlag	Binary Solar Intrusion Flag	240 x `n_scans` x 12	unitless
timeC	Time of Cold Calibration Scan	`n_scans` x 1	seconds
Gain_KpDN	Gain	`n_scans` x 12	K/DN
TC	Deep Space Temperature	`n_scans` x 12	K
encoderAngle_deg	Encoder Angle	10 x `n_scans` x 12	deg
indC	Cold Calibration Spot Indices	10 x 1	unitless
moon_theta_F	W and F band Electronic Boresight	240 x `n_scans`	deg
moon_theta_G	G band Electronic Boresight	240 x `n_scans`	deg

2.3 Assessment of TROPICS Lunar Intrusion Measurements

The lunar calibration performance heavily relies on the quality and reliability of the TROPICS lunar observations. Before using said observations, we focus on two factors to assess data quality: antenna beamwidth and pointing.

2.3.1 Beamwidth

TROPICS Pathfinder defines the antenna beamwidth as the Full Width Half Max (FWHM) beamwidth. Each band is defined with cross track (CT) and along track (AT) beamwidths, and the antenna FOV is the ellipse spanning the down and cross track beamwidths. In this work, we refer to antenna beamwidth and FOV in the same manner.

For lunar calibration, we approximate the antenna main beam pattern as a circularly symmetric Gaussian distribution, where the maximum antenna response lies in the center of the antenna beam. Antenna beamwidth affects the antenna response to the Moon and will separately impact the measured and simulated lunar intrusion temperatures.

In addition, Pathfinder's scans cause beamwidth smearing in the CT direction as shown in Figure 2-2. Although there are estimates for smeared beamwidths, there are currently no on-orbit characterizations. Table 2.2 shows the expected antenna beamwidths for all bands.

Table 2.2: Pathfinder Channel Expected FWHM Beamwidths [18]

Band	**Channel**	**Smeared CT (deg)**	**AT (deg)**
W	1	2.9871	2.7456
F	2 - 8	2.4683	2.3177
G	9 - 11	1.8469	1.5083
	12	1.8066	1.4188

If the actual beamwidth is different from the simulated values, then the lunar

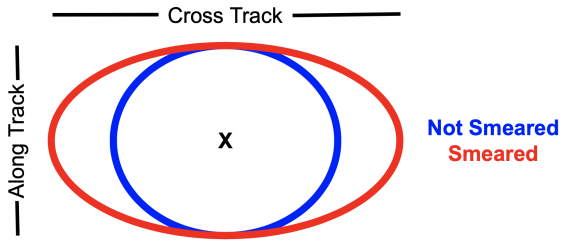

Figure 2-2: An example of an unsmeared and smeared sampling antenna FOV due to Pathfinder's scan pattern, where the center of the FOV is denoted with "X". This smearing increases the effective CT beamwidth. Although there is minor smearing in the along track direction, it is considered negligible compared to the cross track's smearing [19].

calibration results are likely to be affected. If we model the main beam as a circularly symmetric Gaussian distribution, then the estimated lunar temperature will be inflated if the actual beamwidth is larger (with otherwise identical scan geometry). On the other hand, a smaller-than-estimated beamwidth will yield lower lunar temperature estimates.

2.3.2 Pointing

The electronic boresight values in the data fields `moon_theta_F` and `moon_theta_G` are defined as the 1-dimensional, unsigned separation angle between the center of the Moon and the center of the antenna beam (as shown in Figure 2-3). The antenna beam's center relies on spacecraft pointing, so pointing is crucial for lunar calibration. The Moon subtends approximately 0.5° in Pathfinder's FOV, so the measured lunar temperature is sensitive to small pointing fluctuations. Depending on the pointing fluctuations, the Moon can be unexpectedly in or out of the antenna's beamwidth. In either case, the antenna response to the Moon (and therefore Pathfinder's measured antenna temperature) can be affected. In this work, we consider pointing to be affected by three main factors: (1) encoder angle, (2) spacecraft attitude, and (3) antenna beamwidth alignment.

Encoder Angle The encoder angle physically relates to the satellite scan angle. This field is used in coordinate system transformations to calculate the antenna line

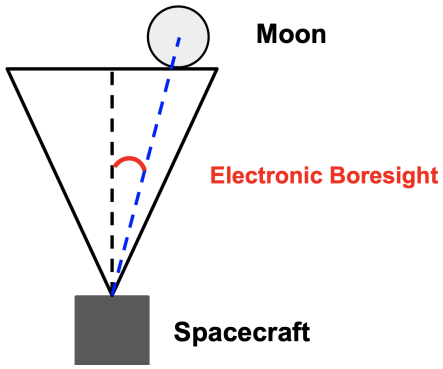

Figure 2-3: A 2-dimensional visualization of the electronic boresight definition. The triangle represents the antenna beam. The black dotted line is the center of the antenna beam (which is also the line of sight), while the blue dotted line connects the antenna to the center of the Moon. The electronic boresight (red) represents the angle between the Moon and the line of sight.

of sight for both the W/F and G bands as described in Appendix B. These line of sight vectors are different for the W/F and G bands due to the differing antenna and receiver chains as shown in Figure 2-4.

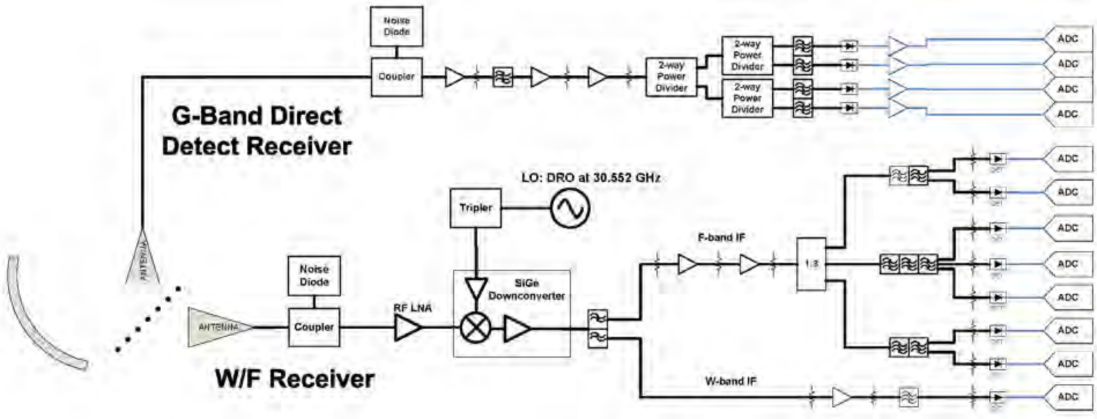

Figure 2-4: A simplified block diagram of the TROPICS payload [18]. The W/F and G bands use different receiver chains and antennas.

The encoder angle is measured using a rotating encoder wheel. For one entire scan, the encoder wheel makes one revolution. While the wheel rotates, the spacecraft measures the encoder angle using the wheel's markings at 15 equally spaced sample encoder angle landmarks. All other encoder angle values and sample times are spline interpolated using these landmarks [18]. Ideally, the encoder angle should smoothly change as the wheel rotates. However, this angle can jitter if the wheel's controller

oscillates at the desired encoder angle. As shown in Figure 2-5, these oscillations can affect the antenna FOV, moving the Moon into and out of the antenna beam and creating fluctuations in measured antenna temperature during lunar intrusions. Section 3.4.1 further describes how encoder angle jitter can affect the data preparation for Pathfinder's lunar observations.

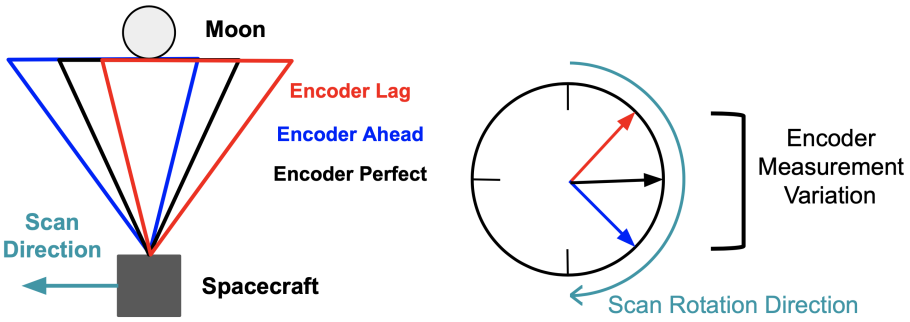

Figure 2-5: An example of encoder angle error and its effects on lunar observations. On the left image, the triangles represent the antenna beam with a lagging encoder (red), an ahead encoder (blue) and a perfect encoder (black). The right plot is a visualization of the encoder measurement variation on the encoder wheel, where the desired encoder angle is the black arrow, and encoder angle jitter is represented by the blue and red arrows. The scan direction indicates the rotational direction of the encoder wheel and spacecraft pointing.

Spacecraft Attitude Spacecraft attitude is defined in terms of roll, pitch, and yaw. As shown in Figure 2-6, deviations in any of these values will induce an offset in antenna FOV orientation and affect the measurement, so the measured antenna temperature during a lunar intrusion with attitude jitter will be different from measurements with perfect attitude because of the different spacecraft orientation.

Antenna Beam Alignment Antenna beam misalignment can be caused by instrument mounting error [18]. Although prelaunch mechanical testing was performed on TROPICS Pathfinder to calculate antenna beam offsets, thermal changes during and after launch can contribute to additional alignment offsets.

As shown in Figure 2-7, antenna beam misalignment changes the location of the antenna field of view with respect to the spacecraft body frame. This misalignment can induce a time offset between when the spacecraft expects there to be a lunar

intrusion and when it actually measures the lunar intrusion. In addition, the antenna response will also be shifted in time.

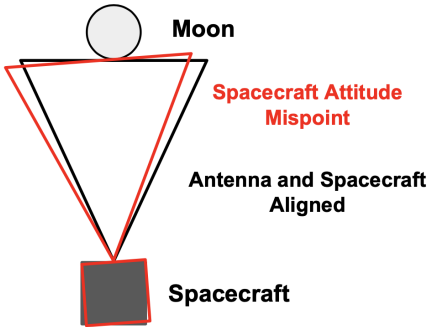

Figure 2-6: An example of spacecraft attitude error and its effects on lunar observations. The triangles represent the antenna beam with attitude error (red) and without pointing error (black).

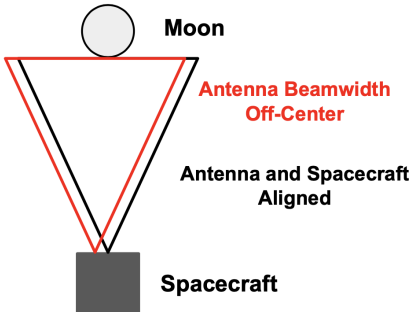

Figure 2-7: A visualization of antenna beamwidth alignment, where the triangles represent the antenna beam when perfectly aligned (black) and off-center (red).

2.4 Summary

To consider lunar calibration, we compare TROPICS Pathfinder lunar observations to Yang and Burgdorf's RTM. In doing so, we assess TROPICS data, focusing on how pointing and beamwidth can affect calibration results. Before comparing TROPICS Pathfinder measured brightness temperature to Yang and Burgdorf's simulated brightness temperatures, we need to preprocess the TROPICS data to estimate measured lunar brightness temperature. Chapter 3 describes our TROPICS data preparation strategy.

Chapter 3

TROPICS Pathfinder Data Preparation

TROPICS lunar intrusion observations must be preprocessed before they can be used for calibration. This chapter covers this preparation workflow, starting from the TROPICS Level 1 data in Section 2.2.

3.1 Calculating Antenna Temperature from Digital Counts

To calculate the antenna temperature corresponding to given digital counts in scan i, we perform the conversion

$$T_A = T_{ds} + G_i * (DN - \overline{DN_i}) \tag{3.1}$$

where T_{ds} is the known deep space temperature as specified in Table 1.3, and G is the gain value for scan i in Kelvin / DN. The input digital counts are DN, and $\overline{DN_i}$ is the median of the 10 cold calibration digital counts for scan i, *excluding* samples flagged as being a solar intrusion by `intruSolarFlag` or other outlier by `cC_CalFlag` from Table 2.1.

In Figure 3-1, we use Equation 3.1 to calculate the digital counts and equivalent

antenna temperature for data from Orbit 1410, Channel 12. Both the digital counts and equivalent antenna temperatures are displayed as 2-dimensional images.

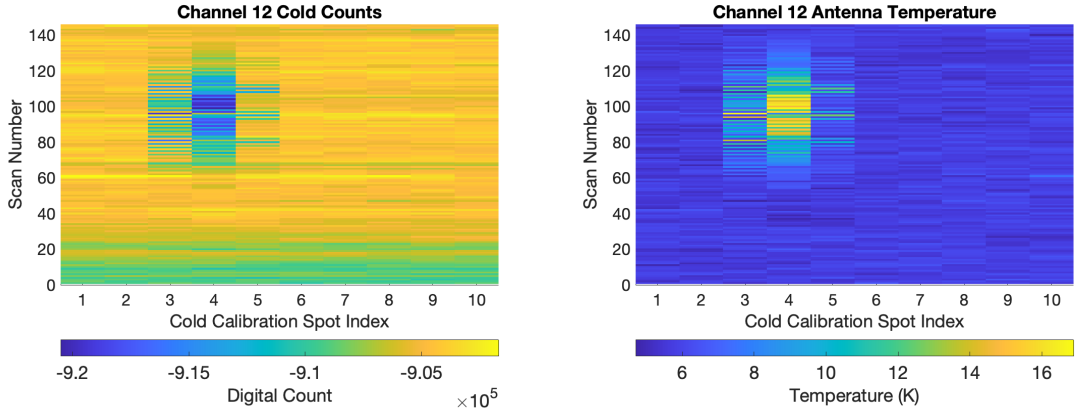

Figure 3-1: The cold calibration digital counts and antenna temperatures for Orbit 1410's channel 12 lunar intrusion observation. This measurement was taken on October 2nd, 2021 when the Moon was a waning crescent with 22% illumination and a phase angle of 117.28° [3, 17].

3.1.1 Channel Variability

Antenna temperatures calculated from Equation 3.1 are channel-specific. This behavior is due to the band-wise and channel-wise variation in inputs such as the deep space temperature, gain, digital counts, and lunar intrusion flags.

The deep space temperature is unique and stable for microwave frequencies, with values calculated using a modified Planck correction and a modified Rayleigh-Jeans approximation [18]. Table 1.3 displays these channel-specific temperatures.

The gain G is calculated as the slope between the deep space and noise diode calibration points for each scan as shown in Figure 1-2. Given that each frequency has a unique deep space temperature, the gain will also vary by channel and will affect the derived antenna temperatures.

3.2 Detecting Lunar Intrusions

The lunar intrusion flags provided in the TROPICS Pathfinder observations (`intruLunarFlag` in Table 2.1) determine if the Moon is in the antenna FOV solely by using spacecraft ephemeris and antenna pointing data, determining if the condition

$$\beta < \overline{BW} + \phi_M/2 \tag{3.2}$$

is true. In Equation 3.2, $\overline{BW}$ is the mean antenna beamwidth between the AT and smeared CT beamwidths given in Table 2.2, β is the electronic boresight, and ϕ_M is the angle subtended by the Moon with respect to TROPICS Pathfinder.

Assuming TROPICS Pathfinder pointing data are accurate, Equation 3.2 would be a reliable (albeit conservative) way to detect lunar intrusions. As $\overline{BW}$ is FWHM, Equation 3.2 requires that the center of the Moon is at least $(\overline{BW})^\circ$ away from the antenna FOV rather than $(\overline{BW}/2)^\circ$. However, as mentioned in Section 3.4, Pathfinder's pointing dataset has offsets and therefore needs to be adjusted. The provided lunar intrusion flags, in turn, also experience this offset and may not accurately capture the lunar intrusion signal.

For instance, take the example in Figure 3-2, which displays the flagged temperature measurements in Channel 12 of Orbit 1410. Given that the Moon's temperature is 2 magnitudes greater than the deep space temperatures in Table 1.3, we expect more photons and a higher measured antenna temperature when the Moon is in the antenna FOV. Although `intruLunarFlag` does flag most of the signal as an intrusion, there appears to be a time offset between the lunar intrusion time period and the time period labeled by `intruLunarFlag`. Specifically, the latter half of the lunar intrusion temperature signal is not flagged, while samples before the temperature are. In addition, low temperature measurements near the frequency-dependent deep space temperature are still flagged as having the Moon in the FOV, even though temperature measurement suggests otherwise. Channel 12, having the smallest antenna beamwidth of all TROPICS channels, is most affected by the offset in `intruLunarFlag` because the lunar intrusion signal (as determined by antenna

temperature measurements) will have the shortest duration.

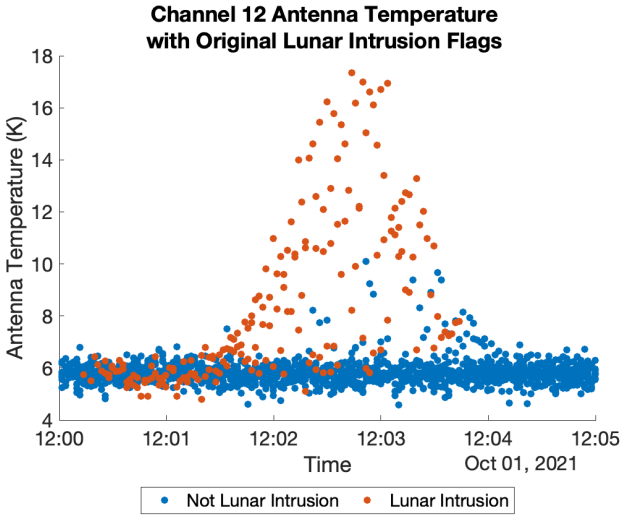

Figure 3-2: The measured antenna temperatures for Channel 12 of Orbit 1410 during a lunar intrusion. The orange points are those flagged by the original TROPICS Pathfinder lunar intrusion flags (`intruLunarFlag` in Table 2.1).

The performance of the Markov Chain Monte Carlo (MCMC) fitting in Section 3.6 depends on how much of the lunar intrusion signal is captured. Therefore, we detect lunar intrusions by analyzing Pathfinder's measured temperatures in addition to considering pointing data.

In order to use a measurements for lunar calibration, we require that:

1. The measurement is not a solar intrusion as flagged by the field `intruSolarFlag` from Table 2.1. Solar intrusions will have high antenna temperatures that may not be physically possible in a lunar intrusion.

2. In addition, after considering (1), the measured antenna temperature must be substantially higher than "uncontaminated" deep space measurements. We thus assume that if the Sun is not in the antenna FOV, then the Moon must be the cause of such an increase in measured antenna temperature in the cold calibration sector.

To meet (1), we exclude all temperatures that are flagged by `intruSolarFlag`. We then satisfy (2) by determining if there remains a high antenna temperature signal. Our method is outlined in Section 3.2.1.

3.2.1 Detecting the Lunar Intrusion Signal

After we exclude all solar intrusion measurements, we assume that any remaining high antenna temperature signals are due to lunar intrusions. We also assume "uncontaminated" deep space temperature measurements are normally distributed and centered on the deep space temperature in Table 1.3.

To detect a lunar intrusion peak, we first characterize the noise σ_{ds} in the Pathfinder cold calibration temperature measurements. By doing so, we can determine what is considered a high temperature measurement. To find σ_{ds}, we create a sliding window over all measured antenna temperatures in a given orbit and then calculate the standard deviation in temperature for each window, which we define as

$$\sigma_{ds,j} = \sqrt{\frac{\sum (T_{A,i} - \mu_j)^2}{N_j}} \tag{3.3}$$

such that, for a given window j, $\sigma_{ds,j}$ is the standard deviation in measured antenna temperature, N_j is the number of samples, $T_{A,i}$ is the i^{th} antenna temperature, and μ_j is the mean antenna temperature. This sliding window is 20 scans wide, which equates to $N_j = 200$ measurements per window.

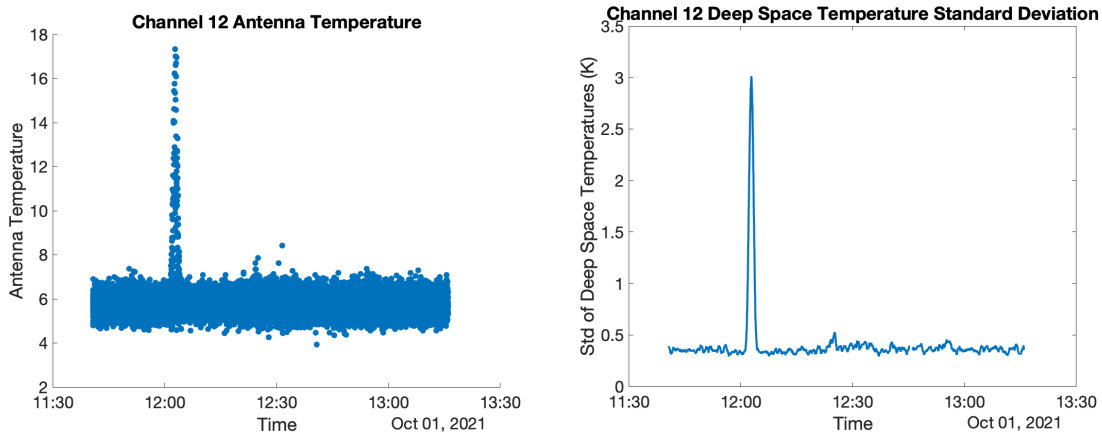

Figure 3-3: A comparison of Orbit 1410 Channel 12 antenna temperatures (left) and corresponding sliding window temperature standard deviations (right). The spike in temperature near 12:00 is the lunar intrusion shown in Figure 3-2. The standard deviation is approximately 0.3582 K for "uncontaminated" measurements.

As shown in Figure 3-3, the window standard deviation increases sharply in the same time period as the lunar intrusion. Besides this time period, the antenna temperature and its standard deviation stay approximately constant. We find σ_{ds} by calculating the median of all window standard deviations in each TROPICS Pathfinder orbit.

In addition to calculating σ_{ds}, we use the sliding window's standard deviation as indicators of a lunar intrusion signal. This indicator is useful in reducing false positives when assigning lunar intrusion flags in Section 3.2.2, particularly in especially noisy temperature measurements. As noted in Figure 3-3, the window standard deviation increases sharply with a lunar intrusion signal. Therefore, we conclude that there is a lunar intrusion signal if the maximum window standard deviation $\sigma_{ds,max}$ satisfies the condition

$$\sigma_{ds,max} > 1 \text{ K} \tag{3.4}$$

The threshold of 1 K is determined empirically. Higher $\sigma_{ds,max}$ indicates some sample window included high measured lunar intrusion temperatures. For lunar calibration, we prefer higher lunar intrusion temperatures because they typically correspond to a more noticeable lunar intrusion signal compared to "uncontaminated" measurements and background noise. These larger signals are easier for MCMC to fit to for lunar calibration in Sections 3.7 and 3.8. Therefore, we prefer using lunar intrusions that have high $\sigma_{ds,max}$ for lunar calibration. Of course, too high of a threshold will exclude too many measurements, reducing the number of points for lunar calibration. We therefore set the threshold to 1 K to balance between these effects.

3.2.2 Assigning Lunar Intrusion Flags

If there is a lunar intrusion signal as indicated by Section 3.2.1, we can then assign lunar intrusion flags based on measured antenna temperature. We set a minimum temperature threshold of

$$T_A > T_{ds} + 4\sigma_{ds}, \tag{3.5}$$

where T_A is the measured antenna temperature, T_{ds} is the deep space temperature from Table 1.3, and σ_{ds} is the noise of the "uncontaminated" deep space temperature measurements. Any measurements that satisfy Equation 3.5 are flagged as lunar intrusions.

Using Equation 3.5, we find the peak of the lunar intrusion signal. Figure 3-4 continues with the Orbit 1410 Channel 12 example from Figure 3-3.

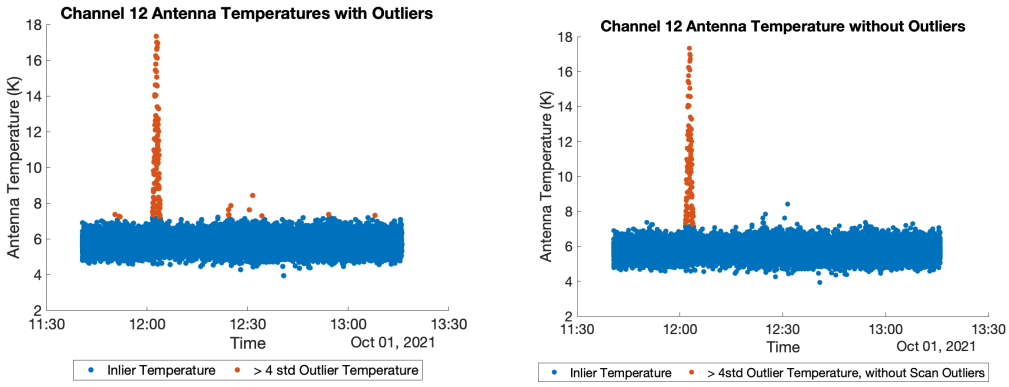

Figure 3-4: The flagged measured antenna temperatures for Orbit 1410 Channel 12 using Equation 3.5 before excluding time outliers (left) and after excluding time outliers (right).

As shown in the left plot in Figure 3-4, the threshold from Equation 3.5 captures most of the lunar intrusion signal but also includes some high, "uncontaminated" measured antenna temperatures. We therefore exclude outlier samples if their sample times are not within the range

$$\bar{t} \pm 3\sigma_t \tag{3.6}$$

to produce the right plot in Figure 3-4. In Equation 3.6, $\bar{t}$ is the mean sample time of all flagged temperature measurements from the left plot in Figure 3-4. Also, σ_t is the

standard deviation of the flagged sample times. The remaining time period covering these flagged sample times can be considered the lunar intrusion time period.

As a note, we use $4\sigma_{ds}$ in Equation 3.5 to reduce the amount of high, "uncontaminated" measured antenna temperatures that are initially flagged. In this way, the time period where the intrusion occurs is more clear, and we can more easily isolate the lunar intrusion signal.

Upon focusing on the lunar intrusion time period, however, we find that the flags in the right plot in Figure 3-4 do not capture the leading or trailing ends of the lunar intrusion signal. This behavior is likely because the Moon is just entering or exiting the antenna FOV, so it thus does not increase the measured temperature enough to satisfy Equation 3.5.

To incorporate the leading and trailing ends, we then expand the lunar intrusion time period by a buffer of 1 minute (or 30 scans) on both ends of the time period. We relax our minimum temperature requirement to be

$$T_A > T_{ds} + 3\sigma_{ds}, \tag{3.7}$$

where T_A, T_{ds}, and σ_{ds} are defined identically to those in Equation 3.5.

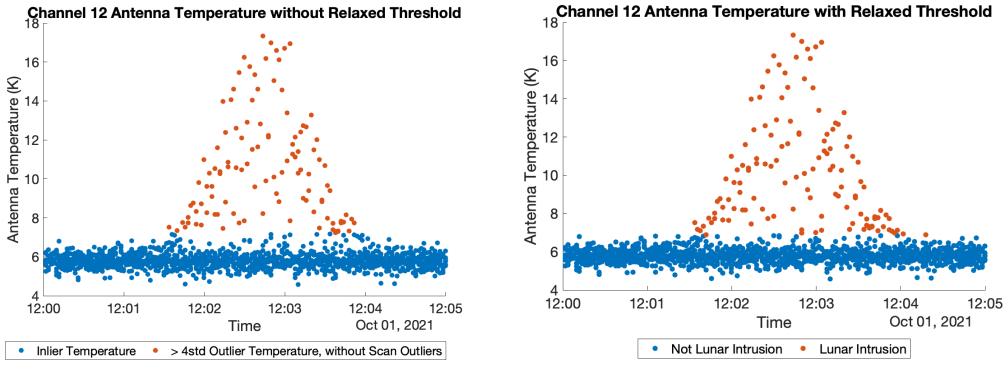

Figure 3-5: The flagged measured antenna temperatures for Orbit 1410 Channel 12 before (left) and after (right) including the 30 scan buffer and relaxed the temperature threshold using Equation 3.7.

As shown in Figure 3-5, using Equation 3.7 allows us to capture more high temperature measurements where the Moon begins to enter the antenna FOV. After relaxing

our threshold, we are able to flag more of the lunar intrusion signal. We refer to the resulting flags as the "custom lunar intrusion flags" in Figure 3-6.

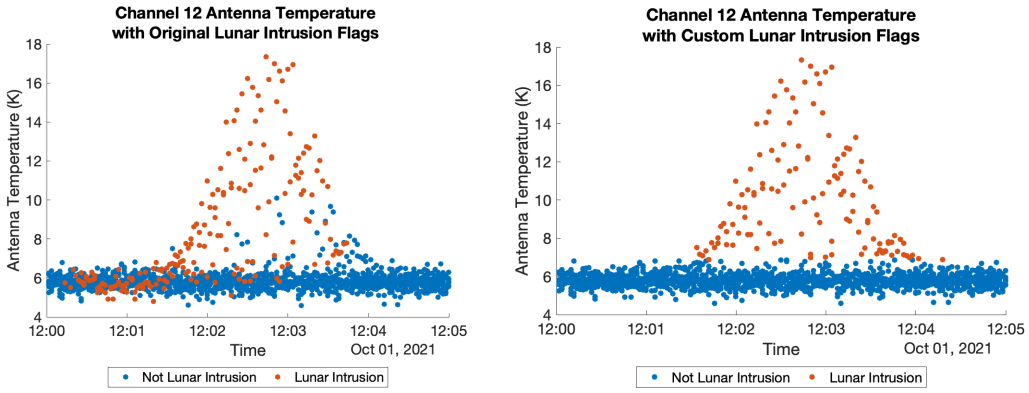

Figure 3-6: A comparison between the original lunar intrusion flag (left) and custom lunar intrusion flag (right) for Orbit 1410 Channel 12 antenna temperatures.

Figure 3-6 demonstrates that the custom lunar intrusion flags better capture the lunar intrusion signal and exclude low temperature measurements from the lunar intrusion. For this thesis, we use the custom lunar intrusion flags as calculated in this section.

3.3 Antenna-Related Equations

Once we detect and flag lunar intrusions in Section 3.2, we then account for pointing error in the TROPICS Pathfinder observations in Section 3.4 and calculate Pathfinder's lunar temperature estimate in Sections 3.6 through 3.8.

In particular, Sections 3.4 and 3.8 rely on antenna-related equations. We outline these equations in this section. These equations are based on the calibration algorithm developed by Crews [9].

The measured antenna temperature during a lunar intrusion can be modeled as

$$T_A = T_{ds} + R \cdot f \cdot T_{moon} \tag{3.8}$$

where T_{ds} is the known deep space temperature, a frequency-dependent value. Table 1.3 displays these known values. R is the normalized antenna response that accounts

for the Moon's position relative to the antenna line of sight. This value is defined in [9] and is

$$R = e^{-\beta^2/(2\sigma^2)} \tag{3.9}$$

such that β is the electronic boresight, and

$$\sigma = \frac{0.5BW}{\sqrt{2\ln 2}} \tag{3.10}$$

Figure 3-7 displays the relationship between β and R. As β increases, the antenna response R decreases as the Moon is further from the center of the antenna FOV.

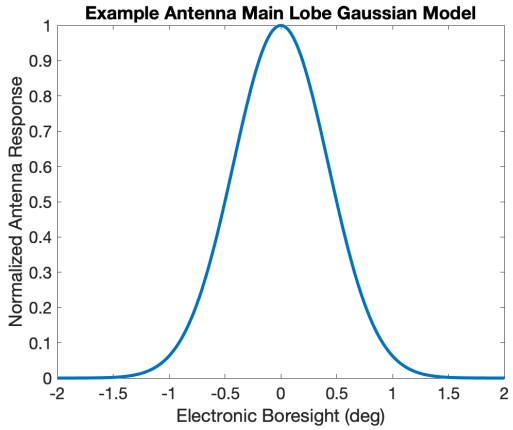

Figure 3-7: An example 2D Gaussian modeling of an antenna main lobe with an antenna beamwidth of 1°. The normalized antenna response R is at its maximum at the center of the antenna FOV.

As an aside, we set the antenna beamwidth BW to be the average of the cross track and along track beamwidths from Table 2.2. These average antenna beamwidths are displayed in Table 3.1.

Table 3.1: The average of the TROPICS Pathfinder Smeared CT and AT antenna beamwidths

Channel	**Smeared CT (deg)**	**AT (deg)**	**Average Beamwidth (deg)**
1	2.9871	2.7456	2.8663
2-8	2.4683	2.3177	2.3930
9-11	1.8469	1.5083	1.6776
12	1.8066	1.4188	1.6127

The value f represents the fill factor, which accounts for the relative size of the Moon with respect to the antenna's field of view. This value is defined as

$$f = \frac{\Omega_M}{\Omega_A} \tag{3.11}$$

such that Ω_M, the solid angle of the Moon, is

$$\Omega_M = \int_0^{2\pi} \int_0^{\phi_M/2} F_{nML}(\theta, \phi) \sin\theta d\theta d\phi \tag{3.12}$$

and Ω_A, the solid angle of the antenna, is

$$\Omega_A = \frac{1}{\eta_{ML}} \int_0^{2\pi} \int_0^{2\pi} F_{nML}(\theta, \phi) d\Omega \tag{3.13}$$

In Equations 3.12 and 3.13, ϕ_M refers to the angle subtended by the Moon, and η_{ML} is the antenna main beam efficiency. The expected main beam efficiencies that are also used in this algorithm are listed in Table 3.2.

Table 3.2: The Expected Main Beam Efficiencies for TROPICS Pathfinder [18]

Channel	**Beam Efficiency (%)**
1	81.15
2	91.70
3	93.80
4	94.10
5	94.30
6	94.60
7	95.60
8	95.40
9	89.10
10	88.50
11	89.70
12	91.90

In addition, F_{nML} is the antenna main beam function given a zenith angle θ, azimuth ϕ, and antenna beamwidth BW from Table 3.1. This function is approximated as a Gaussian of the form

$$F_{nML}(\theta, \phi) = e^{-\ln(2)(2\theta/BW)^2} \tag{3.14}$$

3.4 Accounting for Pointing Error in TROPICS Pathfinder Observations

As mentioned in Section 2.3.2, pointing error in TROPICS Pathfinder can heavily impact the measured antenna temperature during a lunar intrusion and therefore lunar calibration overall. As shown in Figure 3-8, there is some pointing error in TROPICS Pathfinder measurements. For a lunar intrusion, we expect to measure a higher temperature when the Moon is closer to the center of the antenna FOV. This event coincides with an electronic boresight β that is near 0°. As the Moon moves further away from the antenna FOV center, the measured temperature should decrease and approach the frequency-dependent deep space temperature in Table 1.3. In fact, once $\beta > BW/2$, the antenna temperature should be approximately that of deep space as the Moon exits the antenna FOV.

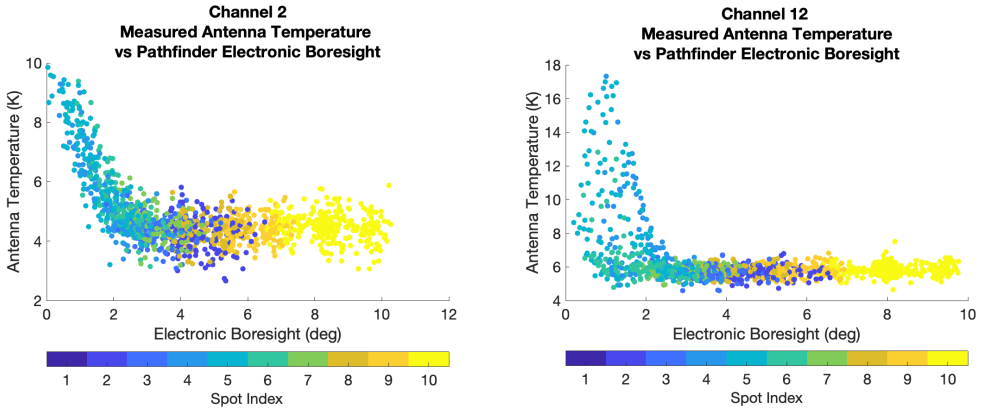

Figure 3-8: The relationship between the measured antenna temperature and the electronic boresight as measured by Pathfinder for Channel 2 (left) and Channel 12 (right).

As mentioned in Section 2.3.2, the W/F bands (Channels 1-8) use a different antenna than the G band (Channels 9-12). Therefore, the G band has a different antenna line of sight (and electronic boresight) from the W/F bands. Even so, Figure 3-8 indicates that there is an angle offset for both bands. Although the antenna temperature approaches the deep space temperature for large β values, the relationship between temperature and electronic boresight is unclear in both plots for smaller β values. In fact, Channel 12's relationship is particularly vague. With a cross-track antenna beamwidth of 1.8066° (as mentioned in Table 2.2), the Channel 12 antenna temperatures should be approximately that of deep space when $\beta > 0.9033°$. However, we see temperatures as high as 10 K for $\beta > 2°$.

As outlined in Section 2.3.2, antenna beamwidth misalignment, spacecraft attitude error, and encoder angle deviations can all cause this behavior. Section 3.4.1 outlines the encoder angle jitter, and Section 3.4.2 details how we calculate the angle offset to account for TROPICS Pathfinder's pointing error.

3.4.1 Encoder Angle Measurements

As described in Section 2.3.2, encoder angle jitter (if present) can contribute to TROPICS Pathfinder's pointing error, later affecting the reliability of lunar calibration. We analyze an example of Pathfinder's encoder fluctuations in Figure 3-9, which occurred on October 30th, 2021 for Spot 1 of the cold calibration sector.

Ideally, the encoder angle should smoothly change as the payload rotates for Sun tracking; however, the encoder angle fluctuates with an amplitude of approximately 1°. In addition to the encoder jitter effects outlined in Section 2.3.2, the 1° jitter appears to also affect our upcoming MCMC fitting for electronic boresight as outlined in Section 3.7. The MCMC fit results rely on how the electronic boresight evolves over time, so any fluctuations in electronic boresight can affect the fit. For instance, higher than expected electronic boresights are particularly influential near the fit's minimum point and often lead to inflated estimates of the minimum electronic boresight. This higher electronic boresight will thus lead to higher lunar temperature estimates.

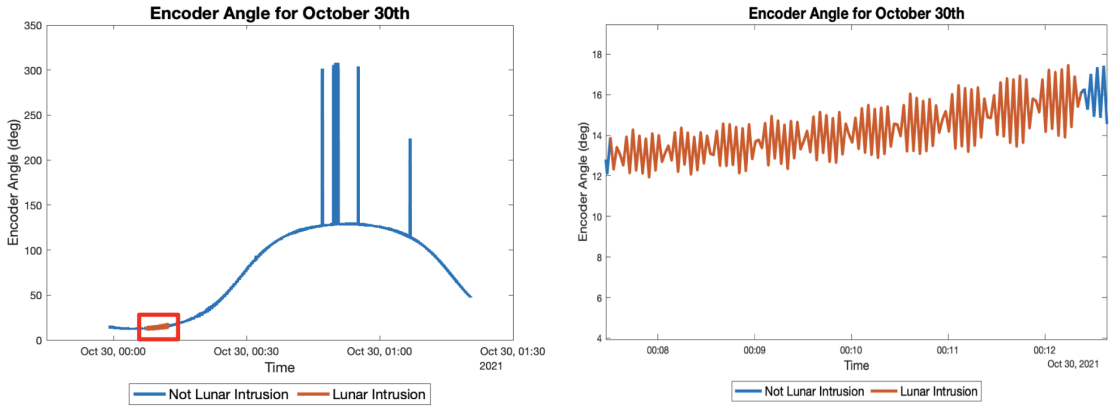

Figure 3-9: The encoder angle values for Spot 1 of the cold calibration sector on October 30th, 2021. The left image displays these values over a single orbit, with the red box surrounding the area that is focused on in the right plot. The gradual change in encoder angle is due to the standard movement of the payload scanner compared to the payload rotation so that the solar array tracks the Sun. The sudden spikes in the left plot are likely due to active spacecraft maneuvers and are not analyzed in this work.

3.4.2 Calculating Angle Offsets

To account for Pathfinder's pointing error, we calculate an angle offset $\Delta\beta$ such that

$$\Delta\beta = \beta - \beta_{truth}, \tag{3.15}$$

where β is the Pathfinder electronic boresight provided in the fields `moon_theta_F` and `moon_theta_G` in Table 2.1 and β_{truth} is the correct electronic boresight. By calculating $\Delta\beta$, we can correct our electronic boresight to be

$$\beta^* = \beta - \Delta\beta, \tag{3.16}$$

where β^* is referred to as the adjusted electronic boresight.

To find $\Delta\beta$ in Equation 3.15, we need to know β_{truth}. However, we do not know this value. We instead turn to Yang and Burgdorf's lunar simulation to calculate β_{sim} (the simulated electronic boresight) and approximate $\beta_{sim} \approx \beta_{truth}$. We outline this approach in Section 3.4.3.

3.4.3 Calculating the Simulated Electronic Boresight β_{sim}

To calculate the simulated electronic boresight β_{sim}, we assume TROPICS Pathfinder's temperature measurement is correct and that the Moon's brightness temperature is equal to Yang and Burgdorf's simulated temperature. We then find the corresponding electronic boresight β_{sim} for these temperatures.

For reference, we restate Equation 3.8 as

$$T_A = T_{ds} + R * f * T_{moon}$$

and reformulate Equation 3.9 as

$$R = e^{-\beta_{sim}^2/(2\sigma^2)}.$$

To find β_{sim}, we therefore set T_{moon} to the lunar brightness temperature from Yang and Burgdorf's RTM and T_A to the measured Pathfinder antenna temperature. T_{ds} is taken from Table 1.3.

In doing so, we invert Equation 3.8 to solve for β_{sim}:

$$\beta_{sim} = \sqrt{-2\sigma^2 \ln\left(\frac{T_A - T_{ds}}{fT_{moon}}\right)} \tag{3.17}$$

As β_{sim} must be real, we only calculate a sample's β_{sim} if:

1. $T_A > T_{ds}$, and

2. $fT_{moon} > T_A - T_{ds}$.

As mentioned in Section 3.4, we consider $\beta_{sim} = \beta_{truth}$, adjusting Pathfinder's β using the angle offset in Equation 3.16. Section 3.4.4 outlines how we adjust Pathfinder's β and apply the adjusted values to lunar calibration.

3.4.4 Workflow for Adjusting Electronic Boresight

After calculating β_{sim} in Section 3.4.3, we calculate the angle offset using Equation 3.15 and determine how it relates with Pathfinder's measured antenna temperature T_A, Pathfinder's electronic boresight β, and the lunar phase θ_M.

To do so, we fit a channel-dependent multivariable polynomial to Pathfinder's samples that takes T_A, β, and θ_M as input when calculating the angle offset $\Delta\beta$. We use the MATLAB function `MultiPolyRegress` to find this multivariable polynomial [8].

Using Pathfinder measurements for lunar calibration that were *also* used to calculate $\Delta\beta$ would be circular. If we were to apply $\Delta\beta$ to these measurements, then Pathfinder's measurements would appear to closely match Yang and Burgdorf's simulation. We therefore split the Pathfinder dataset into two sections: (1) Training and (2) Test.

For the Training dataset, we use Pathfinder measurements from October 2021 to calculate $\Delta\beta$ as a function of T_A, β, and θ_M. By using an entire month for training, we cover the entire range of the lunar cycle in our calculations.

Our Test dataset consists of all Pathfinder measurements that do *not* lie in the Training dataset time period. Here, we test the $\Delta\beta$ calculations during training, evaluate performance, and compare Pathfinder's lunar temperature estimates to Yang and Burgdorf's simulation.

Figure 3-10 displays the performance of the multivariable polynomial for the October 2021 dataset. This month's lunar intrusions cover nearly all lunar phases, with gaps only near Full Moon (0°) due to data availability. The model also has a low mean residual value on the order of $(10^{-14})^\circ$ as shown in the second column, with at most 0.1° and 0.2° residual for Channels 2 and 12, respectively. As shown in the right column, the residuals vary depending on the lunar phase. The model's residuals tend to have a larger range near New Moon (±180°), while having a smaller range near Full Moon (0°). This variation may be due to two factors: (1) lunar phase distribution in lunar intrusions, and (2) the higher SNR at Full Moon. With more intrusion sam-

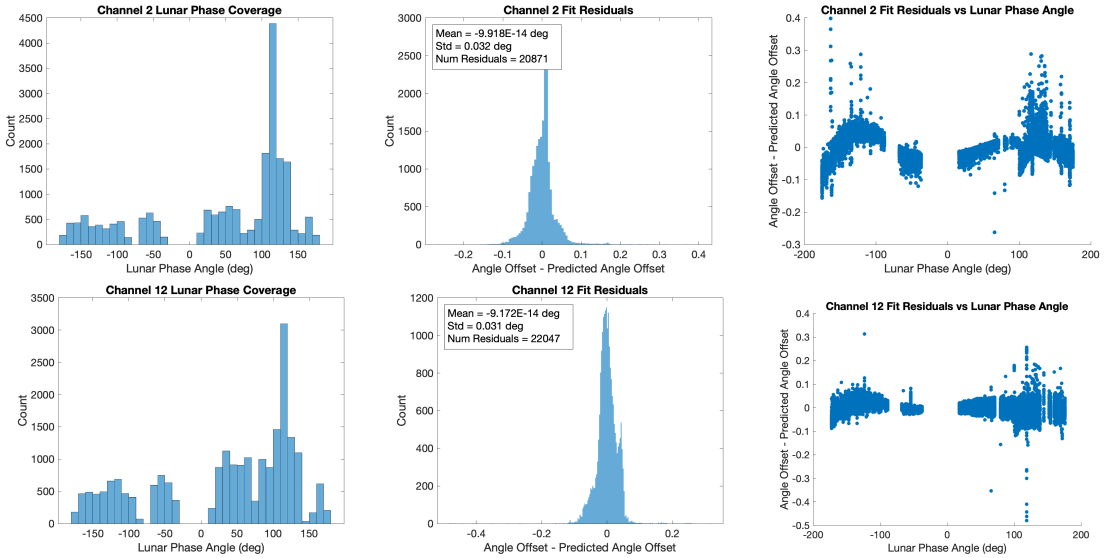

Figure 3-10: The multivariable polynomial fit performance when calculating the angle offset $\Delta\beta$ for Channels 2 (top) and 12 (bottom) in October 2021. The left column shows the distribution of lunar phase angles for the lunar intrusions, while the middle column shows the distribution of $\Delta\beta$ residuals. The right column displays the relationship between the lunar phase and $\Delta\beta$ residuals. $\Delta\beta$ is calculated as "Angle Offset - Predicted Angle Offset," where "Angle Offset" is the angle offset as calculated in the Training dataset, and "Predicted Angle Offset" is the angle offset predicted by the model for the test dataset.

ples at 100° lunar phase angle, for instance, we may get more variation in angle offset residuals. When the Moon is at 0°, we expect a higher intrusion temperature reading, which increases SNR and may help the model's performance. Overall, Figure 3-10 displays current $\Delta\beta$ results. From here onwards, we use the channel-specific models to adjust Pathfinder's electronic boresight, feeding the adjusted electronic boresight into our lunar calibration algorithm starting in Section 3.5.

3.5 Resampling and Smoothing Data

We resample and smooth the data in order to translate the 2-dimensional lunar image (with dimensions 10 x `n_scans`) to a 1-dimensional vector (of length 10 x `n_scans`) and to reduce the noise and fluctuations in the on-orbit measurements. This way, we can perform MCMC fitting as discussed in Section 3.6.

We resample the lunar measurements by using only the maximum lunar intrusion

temperature (and its corresponding electronic boresight) per scan. We resample in this manner because the electronic boresights and measured lunar intrusion temperatures are sensitive to noise and small offsets. To smooth the data, we calculate a moving windowed average lasting 6 seconds, which, in practice, translates to a window of 3 samples wide.

Figure 3-11 displays the resulting values after resampling and smoothing of the intrusion temperatures in Figure 3-1.

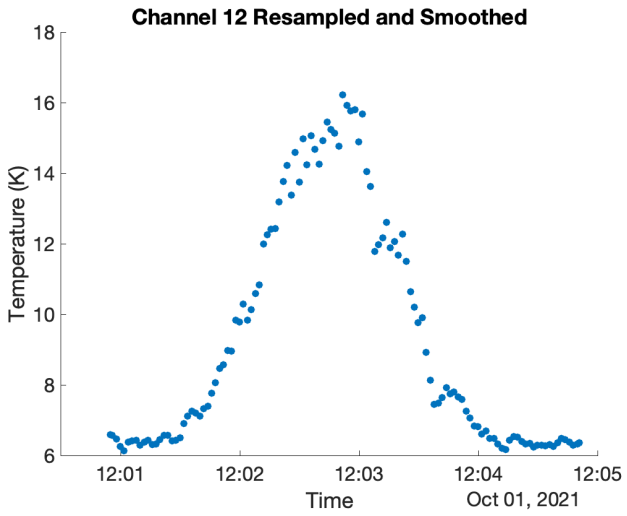

Figure 3-11: The Channel 12 antenna temperature for Orbit 1410 after smoothing and resampling as outlined in Section 3.5.

3.6 Markov Chain Monte Carlo Fitting

Once the data is resampled and smoothed, we perform the Markov Chain Monte Carlo (MCMC) algorithm for data fitting. MCMC is a stochastic algorithm that estimates unknown variables by sampling from their unknown posterior distributions. Instead of independently sampling from these distributions, MCMC creates a Markov chain such that the previous sample's value affects the following one [13]. In doing so, MCMC can converge to multiple variables' final estimates even in large, high-dimensional sample spaces while quantifying uncertainty. MCMC is a valuable strategy given that we are estimating multiple parameters.

The MCMC algorithm has multiple sampling variants. One popular option is the

Metropolis Hastings sampler (MHS), which creates proposed values for variables and determines whether these values are more likely than the current ones.

These proposals Y_i are generated by sampling from:

$$\mathcal{N}(X_i, \sigma_i^2) \tag{3.18}$$

where X_i is the i^{th} variable and σ_i is considered the "step size" of variable i. One proposed value is generated per variable in each iteration, and together, all proposed values in an iteration are considered a proposed set.

The proposed set Y is accepted with probability

$$min(1, \frac{\pi(Y)P(Y)}{\pi(X)P(X)}) \tag{3.19}$$

such that X is the current variable set. The function $\pi(X)$ calculates the probability of measuring the actual values given the variable set X, and $P(X)$ is the probability of the set X given a prior [13]. Priors are situation-specific and will be covered in Sections 3.7 and 3.8.

In the event of an acceptance, the next iteration's variable set is assigned to Y. Else, the variable values are kept the same.

Over many iterations, this MCMC algorithm will converge and oscillate around each variable's final estimates. Because the initial guess for each variable can be far from their respective final estimate, we disregard or "burn-in" the first 20% of samples to minimize erroneous shifts in variable estimates.

3.6.1 Tuning Parameters

Although powerful, MCMC's performance can change dramatically with parameter tuning. The main tunable parameters we focus on are the sample step size σ_i and the total number of iterations.

Ideally, the MCMC algorithm should quickly converge towards its final estimate for each variable while also efficiently exploring the sample space. This balance implies

that the sample step size must be large enough to explore other values, but not too large to greatly delay convergence.

Likewise, we need enough iterations to allow for such sample space exploration and to reliably estimate variables. Not running MCMC long enough means we likely will not have enough information to reconstruct the posterior distribution, while running too long leads to an enlarged run time.

3.6.2 Fit Metrics

To evaluate the performance of the MCMC method, we use three fit metrics: the sample value history, posterior distribution, and marginal distribution. These metrics were also used when tuning the model to increase performance.

Sample Value History

Plotting the sampling history of the MCMC method allows us to evaluate the step size and fit performance. When the algorithm performs well, the sampling history should quickly oscillate around the final variable estimate with roughly constant variance. Having too large of a step size would create abrupt jumps in sample history, whereas too small of a step size would prevent us from aptly exploring the sample space.

Posterior Distribution

When estimating multiple variables, displaying the posterior distribution between two variables is helpful in visualizing fit performance. Ideally, we expect a well-defined 2-dimensional normal distribution such that its peak corresponds to a higher likelihood.

Marginal Distribution

Plotting each variable's marginal distribution allows us to evaluate fit for all variables individually. For good performance, we expect the marginal distribution to be approximately Gaussian; having gaps in the distribution or a non-Gaussian shape is typically indicative of an incorrect step size or not enough iterations.

Apart from evaluating fit, we can extract the final estimate and uncertainty for each variable from the marginal distribution. The final estimate is the mean of the marginal distribution, while the uncertainty is the standard deviation. With these calculations in mind, we prefer a marginal distribution with as low of a standard deviation as possible.

3.7 Estimating Electronic Boresight Angle

To estimate electronic boresight angle as a function of time, we use the MCMC algorithm to fit to

$$\beta(t) = A \cdot \exp[\frac{(B-t)^2}{C^2}] + D \tag{3.20}$$

where t is time.

Our unknown variables are A (the amplitude), B (the center), and C (the spread); D is the maximum angle measurement found in the preprocessed intrusion scans and is thus known.

We formulate our initial guess such that $A = \theta_{min} - D$, where θ_{min} is the minimum electronic boresight angle after the preprocessing in Section 3.5.

For given A and C values during MCMC fitting, our prior will be

$$ne^{|A \cdot C|/475} \tag{3.21}$$

where n is the number of preprocessed measurements. This way, we incentivize the algorithm to use as small of A and C values as possible to closely fit the data.

We run the MCMC algorithm for 50,000 iterations, using the step sizes for A, B, and C as displayed in Table 3.3. We chose these step sizes based on fit performance, particularly the metrics outlined in Section 3.6.2.

Table 3.3: MCMC Electronic Boresight Fit Step Size

Channel	***A***	***B***	***C***
1	0.1	1	1
2 - 12	0.1	1	0.9

After performing MCMC fitting, we estimate the minimum lunar intrusion electronic boresight angle as $A + D$. Figures 3-12 - 3-14 display example results and diagnostics corresponding to inputs from Figure 3-1.

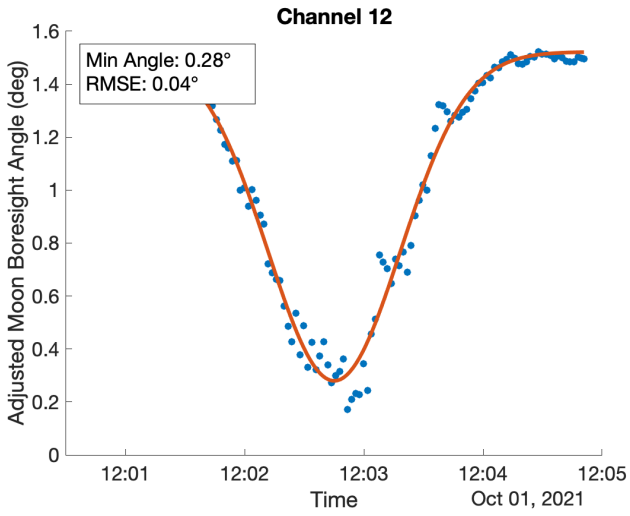

Figure 3-12: The MCMC fit (red) for the Channel 12 electronic boresight in Orbit 1410. The electronic boresight angles (blue) are preprocessed as outlined in Section 3.5, and the minimum electronic boresight from the MCMC fit is 0.28°.

From Figure 3-12, we see that the MCMC model fits the resampled and smoothed electronic boresight angles well, with a root mean squared error (RMSE) of 0.04°. Figure 3-13 demonstrates that the MCMC model is quickly able to converge to this well-fitting model. The marginal distributions for A, B, and C match a Gaussian distribution, and the sample history for each variable quickly oscillate around the mean variable value. This behavior indicates that the step size for each variable is appropriate. We use the mean and standard deviation of each marginal distribution as the variable's final estimate and uncertainty values.

Figure 3-14 further supports the high MCMC fit performance for electronic boresight. The posterior between A and C form a well-defined 2-dimensional histogram with a distinct peak area. In this high-likelihood area, A ranges from $-1.26°$ to $-1.24°$, and C is between 46.7 s and 48 s. These final estimates from Figure 3-13 match these value ranges.

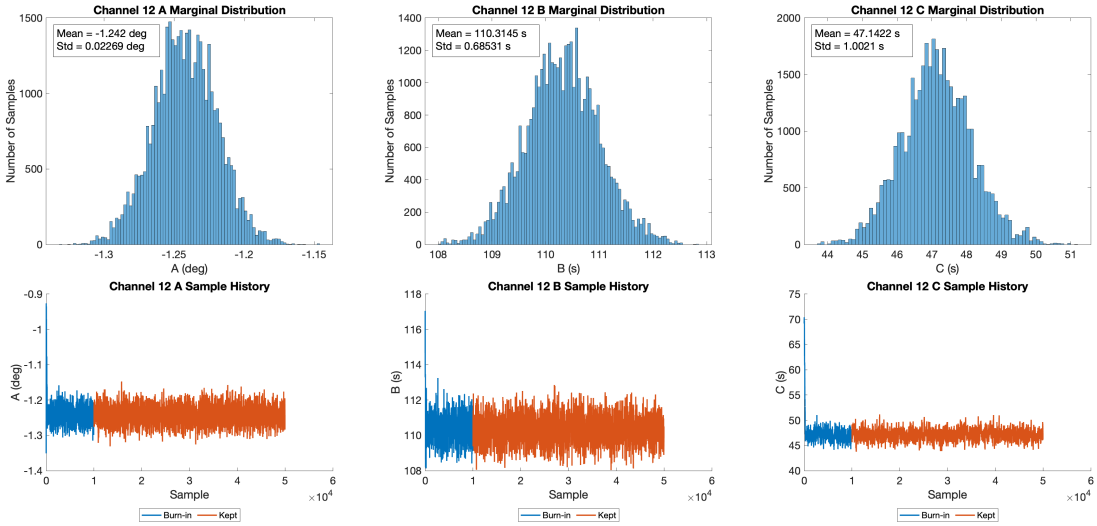

Figure 3-13: The Orbit 1410 Channel 12 MCMC electronic boresight fitting diagnostic plots for amplitude A (left), center B (middle), and spread C (right). The top row shows the marginal distribution for each variable after the burn-in period, and the bottom row displays the corresponding sample history such that the blue area is the burn-in period. The samples in the burn-in period are not used for estimation. The final estimate and uncertainty for A, B, and C are $-1.242° \pm 0.02269°$, 110.3145 s $\pm$ 0.6851 s, and 47.1422 s $\pm$ 1.0021 s, respectively.

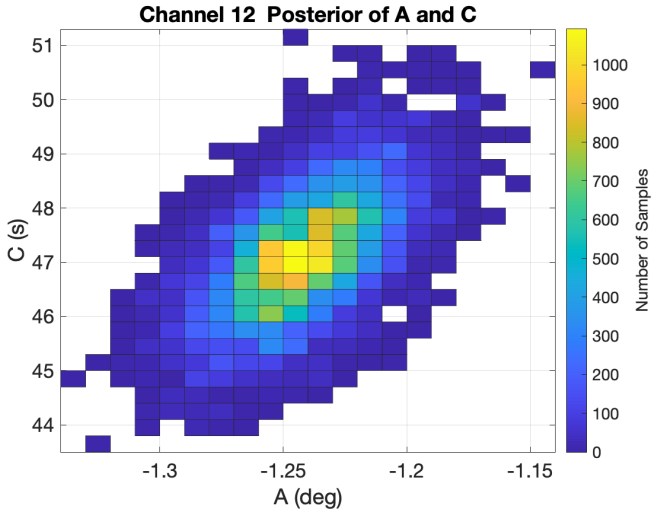

Figure 3-14: The posterior distribution between A (the amplitude) and C (the spread) for Orbit 1410 Channel 12 MCMC electronic boresight fitting. The samples displayed are not part of the burn-in period.

3.8 Estimating Measured Lunar Intrusion Temperature

To estimate the measured lunar intrusion temperature, we use the MCMC algorithm to fit to Equation 3.20. The unknown variables B and C are defined identically to those in Section 3.7. A is in Kelvin, and D is the known channel-specific deep space temperature. Also, our prior is formulated identically to Equation 3.21.

By fitting our measurements to Equation 3.20, we estimate the peak measured lunar intrusion temperature as $A + D$. We run the MCMC algorithm for 50,000 iterations and band-specific step sizes for each unknown variable. These step sizes are listed in Table 3.4.

Table 3.4: MCMC Intrusion Temperature Fit Step Size

Channel	***A***	***B***	***C***
1	0.2	2.5	2.3
2 - 8	0.1	0.9	1.3
9 - 11	0.1	0.5	1
12	0.1	0.5	1

Figures 3-15 through 3-17 display example results and metrics from the fit procedure. Figure 3-15 shows that the resulting MCMC model closely fits the smoothed and resampled measured antenna temperatures with a RMSE of 0.32 K. Indeed, Figure 3-16 also indicates that the MCMC algorithm converges quickly to its final solution. The sampling histories demonstrate that the MCMC sampler quickly oscillates around a single value for each variable. These values and the oscillation amplitude correspond to the mean and standard deviations in marginal distributions in the top row, respectively. The marginal distributions themselves are approximately Gaussian with few sample gaps, indicating the variables' step sizes were appropriate. We use the mean and standard deviation of each marginal distribution as the final estimate and uncertainty for each variable, respectively.

We plot the posterior distribution of A (the signal amplitude) and C (the signal

spread) in Figure 3-17 to assess fit performance. Based on Section 3.6.2, we expect a 2-dimensional histogram with a well-defined "high-sample" region which represents the area of more likely variable values. Figure 3-17 meets our expectation. Generally, A values ranging from 9 K - 9.2 K and C values ranging from 43.5 s - 44.5 s yield better fitting models. These ranges match the A and C estimates in Figure 3-16.

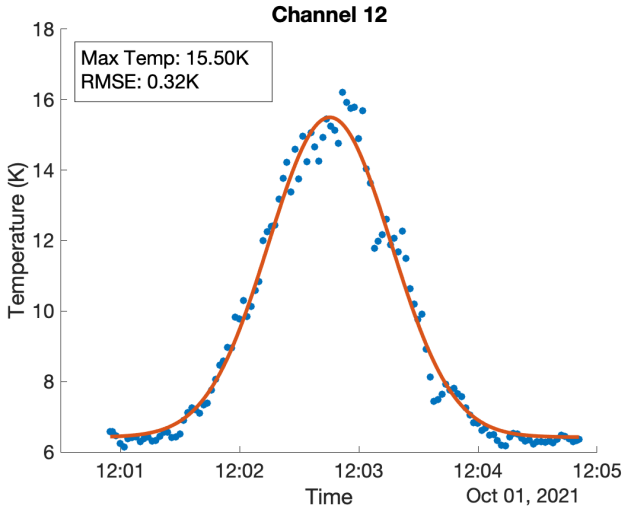

Figure 3-15: The MCMC Gaussian fit (red) for Channel 12 of Orbit 1410. The peak temperature from the MCMC fit is 15.50 K. The preprocessed temperatures in blue are the same as those in Figure 3-11.

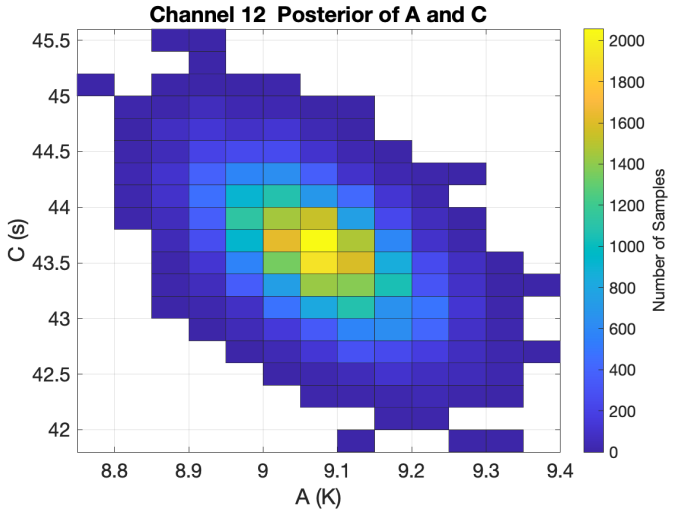

Figure 3-17: The posterior distribution between A (the amplitude) and C (the spread) for Orbit 1410 Channel 12 MCMC temperature fitting. The samples displayed are not part of the burn-in period.

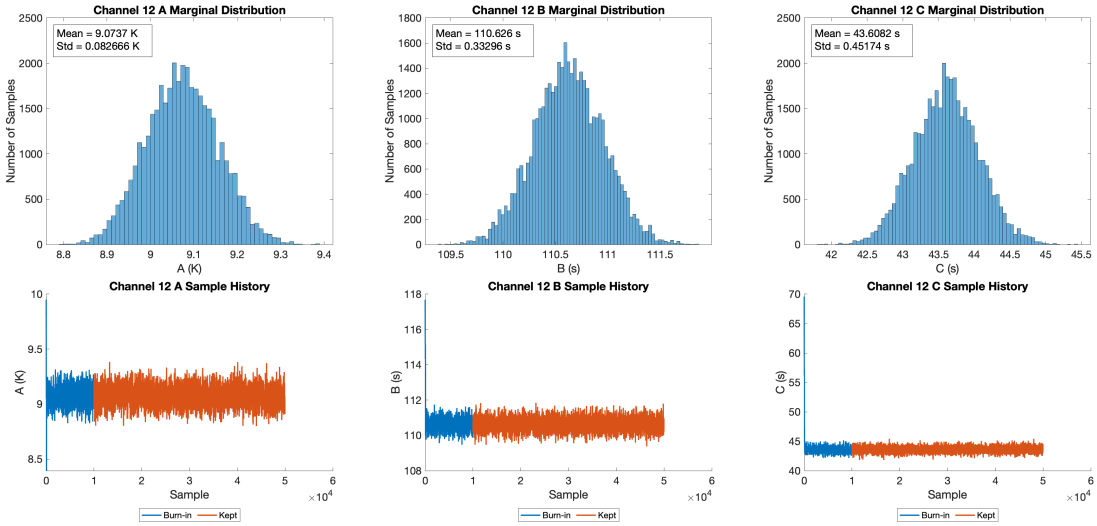

Figure 3-16: The Orbit 1410 Channel 12 MCMC temperature fitting diagnostic plots for amplitude A (left), center B (middle), and spread C (right). The top row shows the marginal distribution for each variable after the burn-in period, and the bottom row displays the corresponding sample history such that the blue area is the burn-in period. The samples in the burn-in period are not used for estimation. The final estimate and uncertainty for A, B, and C are 9.0737 K $\pm$ 0.082666 K, 110.626 s $\pm$ 0.33926 s, and 43.6082 s $\pm$ 0.45174 s, respectively.

3.9 Estimating Measured Lunar Temperature

After estimating the minimum electronic boresight and maximum antenna temperature during a lunar intrusion, we estimate Pathfinder's lunar temperature measurement. To estimate Pathfinder's lunar temperature measurement, we use equations outlined in Section 3.3. We restate Equations 3.8 and 3.9 for reference.

In Equation 3.8, we model the measured antenna temperature as

$$T_A = T_{ds} + R \cdot f \cdot T_{moon},$$

where Equation 3.9 defines R as

$$R = e^{-\beta^2/(2\sigma^2)}.$$

To solve for Pathfinder's lunar temperature measurement T_{moon}, we invert Equa-

tion 3.8 to

$$T_{moon} = \frac{T_A - T_{ds}}{R \cdot f}, \tag{3.22}$$

setting T_A to the maximum MCMC antenna temperature. We calculate R by setting β to the minimum electronic boresight found from the MCMC fitting algorithm. All other inputs are defined identically to those in Section 3.3.

Using Equation 3.22, we calculate Pathfinder's lunar temperature estimates and uncertainties for all of Orbit 1410's channels in Table 3.5 as an example. Our uncertainty calculations are detailed in Section 3.11. We compare the lunar temperature estimates to the simulated lunar temperatures from Yang and Burgdorf's RTM in Chapter 4.

Table 3.5: The lunar temperature estimates for Orbit 1410 compared to the simulated lunar temperature from Yang and Burgdorf's RTM

Channel	**Lunar Temperature Estimate (K)**	**Simulated Lunar Temperature (K)**
1	192.59 ± 12.33	204.58
2	198.26 ± 6.02	198.57
3	192.37 ± 5.93	198.22
4	191.90 ± 6.71	198.06
5	198.46 ± 5.76	197.92
6	202.94 ± 5.45	197.79
7	194.37 ± 7.25	197.69
8	193.54 ± 7.49	197.61
9	190.71 ± 4.64	185.52
10	190.56 ± 4.73	185.22
11	187.55 ± 4.29	184.69
12	178.11 ± 3.96	182.76

As shown in Table 3.5, Pathfinder's lunar temperature estimate is within 10 K of the simulated lunar temperature for all channels except for Channel 1. These differences include all possible causes of model error that are discussed in Section 4.3 and Future Work (Section 5.1. This behavior is likely because Channel 1 has the largest antenna beamwidth and the lowest SNR. Due to the higher noise and the fact that the Moon occupies a lower proportion of the antenna FOV, Channel 1 will typically deviate more from the simulated lunar temperatures. We also see

this pattern in the lunar temperature uncertainties, as Channel 1's uncertainty is approximately 12.33 K, while Channels 9-12 (which are the G band) have uncertainties less than 5 K.

3.10 Calculating Simulated Antenna Temperature

In addition to estimating Pathfinder's lunar temperature measurement, we also calculate the simulated antenna temperature $T_{A,sim}$. This simulated antenna temperature assumes that the disk-averaged lunar brightness temperature is the output of Yang and Burgdorf's RTM. Here, we define this value as $T_{moon,sim}$.

To calculate $T_{A,sim}$, we adapt Equation 3.8 to

$$T_{A,sim} = T_{ds} + R \cdot f \cdot T_{moon,sim}, \tag{3.23}$$

where T_{ds}, R, and f are defined in Equation 3.8. For $T_{A,sim}$, we assume the scan geometry is identical to Pathfinder's, so we use the same electronic boresight estimate from Section 3.7, solid angle ratio f, and beamwidths as in Section 3.9.

Table 3.6 displays the simulated antenna temperatures as well as their uncertainties for all channels in Orbit 1410. The uncertainties for simulated antenna temperature are calculated using Section 3.11, while the uncertainties for the Pathfinder antenna temperatures are taken from the MCMC uncertainties in Section 3.8. With these calculations, we can then compare Pathfinder's measured antenna temperature to the simulated antenna temperature during lunar intrusions.

As shown in Table 3.6, the Pathfinder antenna temperature is quite close to the simulated antenna temperature, with all channels within 0.6 K of the simulated values. The G band (Channels 9-12) has lower uncertainties for Pathfinder antenna temperature than the W/F band (Channels 1-8) likely due to its comparatively higher SNR. However, due to its smaller antenna beamwidths, the G band has larger simulated antenna temperature uncertainty because of its higher sensitivity to small electronic boresight deviations.

Table 3.6: A comparison between the Orbit 1410 Pathfinder peak antenna temperature from MCMC fitting in Section 3.8 and the corresponding simulated antenna temperature

Channel	**Pathfinder Antenna Temperature (K)**	**Simulated Antenna Temperature (K)**
1	9.13 ± 0.15	9.35 ± 0.03
2	9.03 ± 0.09	9.23 ± 0.05
3	8.93 ± 0.09	9.17 ± 0.05
4	8.97 ± 0.11	9.18 ± 0.05
5	9.26 ± 0.10	9.49 ± 0.05
6	9.84 ± 0.11	9.97 ± 0.05
7	8.94 ± 0.12	9.17 ± 0.04
8	9.18 ± 0.14	9.48 ± 0.05
9	13.68 ± 0.08	14.27 ± 0.14
10	13.73 ± 0.09	14.26 ± 0.14
11	14.13 ± 0.08	14.70 ± 0.13
12	15.50 ± 0.08	16.08 ± 0.14

3.11 Quantifying Uncertainty

In addition to calculating Pathfinder's lunar temperature estimate, we calculate the corresponding uncertainty by propagating the MCMC uncertainty through the algorithm in Section 3.9. As we use the MCMC algorithm for both the Pathfinder measurement antenna temperature and the electronic boresight, we have two sets of uncertainty values to propagate. The MCMC electronic boresight uncertainty affects both the Pathfinder lunar temperature estimate and the simulated antenna temperature, while the MCMC antenna temperature uncertainty only affects the Pathfinder lunar temperature estimate. In the following sections, we outline our approach to calculating both sets of uncertainty values.

3.11.1 Uncertainty from the Measured Antenna Temperature

From the MCMC fitting algorithm in Section 3.8, we extract the maximum antenna temperature along with its uncertainty. We define this antenna temperature uncer-

tainty as ϵ_A.

To calculate the contribution of ϵ_A on Pathfinder's lunar temperature estimate (which we denote as $\epsilon_{A,Lunar}$), we use the antenna equations from Section 3.3 such that

$$\epsilon_{A,Lunar} = \frac{\epsilon_A}{R \cdot f}, \tag{3.24}$$

where R and f are defined identically to those in Section 3.3. Figure 3-18 displays the uncertainty $\epsilon_{A,Lunar}$ for October 2021.

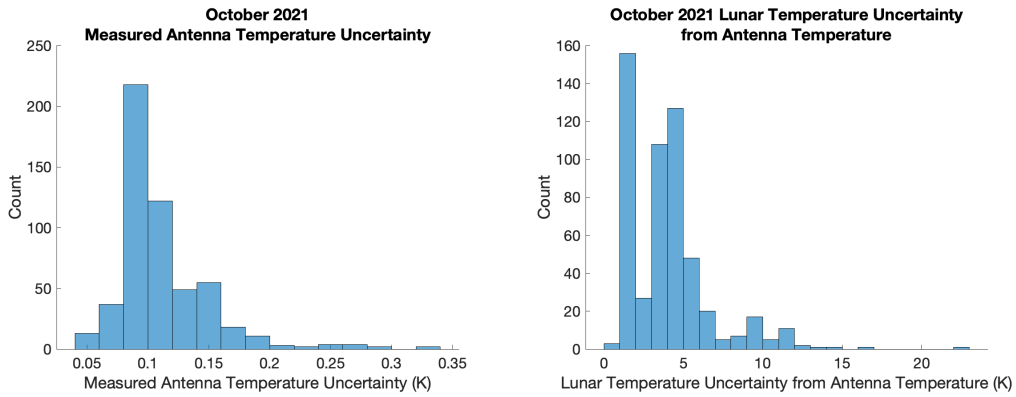

Figure 3-18: The distribution of measured antenna temperature uncertainty from MCMC fitting (left) and the distribution of these uncertainties propagated to lunar temperature uncertainty (right). All values are for all channels in October 2021 lunar intrusions.

Figure 3-18 shows that the measured antenna temperature uncertainty ϵ_A is at most 0.35 K for all lunar intrusions in October 2021, with the majority of uncertainties being less than 0.2 K. When propagated to the TROPICS Pathfinder lunar temperature estimate, these uncertainties reach a maximum of 25 K. This increase in temperature uncertainty is because we divide by the antenna response R and solid angle ratio f, making the lunar temperature uncertainty sensitive to the electronic boresight estimates.

3.11.2 Uncertainty from the Electronic Boresight

Unlike in Section 3.11.1, we cannot use Equation 3.24 to calculate the contributions of the MCMC electronic boresight uncertainty to simulated antenna temperature and

to the Pathfinder lunar temperature estimates. As shown in Figure 3-7, the antenna response R is nonlinear with respect to electronic boresight. Therefore, we characterize how changes in the electronic boresight affect the simulated antenna temperature and the Pathfinder lunar temperature estimate by calculating the derivatives of each with respect to electronic boresight.

In essence, we find the derivative

$$\frac{\mathrm{d}X}{\mathrm{d}\beta} = F(\beta) \tag{3.25}$$

where X is the value we are estimating (either the Pathfinder lunar temperature measurement or the simulated antenna temperature), and $F(\beta)$ is a function dependent on β. Technically, $F(\beta)$ also depends on the channel (using values such as antenna beamwidth and frequency-dependent simulated lunar brightness temperatures). However, the channel-dependent values do not depend on β and are thus considered constants.

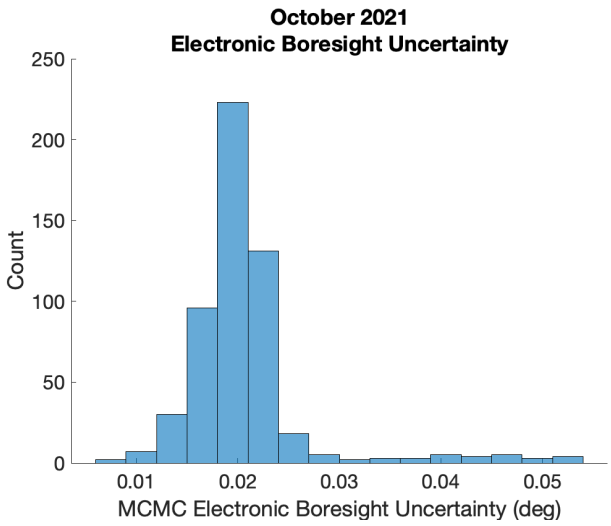

Figure 3-19: The MCMC electronic boresight uncertainty for lunar intrusions in October 2021. All channels' uncertainties are displayed.

As shown in Figure 3-19, the MCMC electronic boresight uncertainties are small, with all values under 0.06° and most approximately 0.02°. Given how small the electronic boresight uncertainty is, we can linearly approximate the slope of the Pathfinder lunar temperature and simulated antenna temperature around the electronic boresight

estimate.

Using this linear approximation, we define the propagated uncertainty as

$$\mathrm{d}X = F(\beta)\mathrm{d}\beta \tag{3.26}$$

This approximation does assume that regardless of how the electronic boresight changes within its uncertainty bounds, the entire Moon remains in the antenna field of view. We therefore filter for lunar intrusions whose MCMC minimum electronic boresight satisfies

$$\beta < \frac{1}{2}(BW - \phi_M) - \mathrm{d}\beta \tag{3.27}$$

where β is the electronic boresight, BW is the antenna beamwidth, ϕ_M is the angle subtended by the Moon, and $\mathrm{d}\beta$ is the MCMC electronic boresight uncertainty.

In the following sections, we define the function $F(\beta)$ formally and outline how we propagate electronic boresight uncertainty to simulated antenna temperature and Pathfinder lunar temperature.

Uncertainty in Simulated Antenna Temperature As the simulated antenna temperature defined in Equation 3.23 depends on the Pathfinder electronic boresight, we analyze how the MCMC electronic boresight uncertainty $\mathrm{d}\beta$ affects the simulated antenna temperature estimates. We restate our equation for simulated antenna temperature from Section 3.10, substituting R for its definition in Section 3.3. Given our Pathfinder electronic boresight β, we define

$$T_{A,sim} = T_{ds} + \exp(\frac{-\beta^2}{2\sigma^2}) \cdot f \cdot T_{moon,sim} \tag{3.28}$$

where σ and f are defined in Section 3.3. We can then calculate $\dfrac{\mathrm{d}T_{A,sim}}{\mathrm{d}\beta}$ as

$$\frac{\mathrm{d}T_{A,sim}}{\mathrm{d}\beta} = \frac{-2}{\sigma^2} \cdot f \cdot T_{moon,sim} \cdot \beta \cdot \exp(\frac{-\beta^2}{2\sigma^2}) \tag{3.29}$$

By multiplying Equation 3.29 by $\mathrm{d}\beta$, we approximate the uncertainty in simulated

temperature $\epsilon_{\beta,Antenna}$ as

$$\epsilon_{\beta,Antenna} = |\mathrm{d}T_{A,sim}| = \frac{2}{\sigma^2} \cdot f \cdot T_{moon,sim} \cdot \beta \cdot \exp(\frac{-\beta^2}{2\sigma^2}) \cdot \mathrm{d}\beta \tag{3.30}$$

As a note, we take the absolute value of $\mathrm{d}T_{A,sim}$ because uncertainty is unsigned. All other factors in Equation 3.30 are positive by definition. Using Equation 3.30, we calculate the uncertainty in simulated antenna temperature for October 2021 lunar intrusions and display its distribution in Figure 3-20.

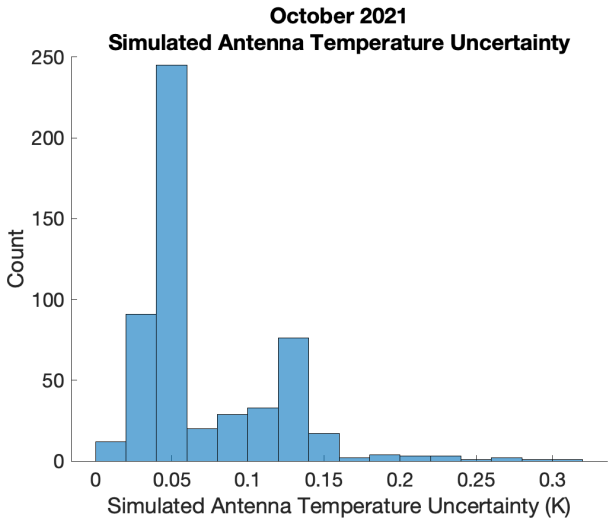

Figure 3-20: The uncertainty in simulated antenna temperature for all channels in October 2021 lunar intrusions as calculated from Equation 3.30.

As shown in Figure 3-20, the simulated antenna temperature uncertainties in October 2021 are at most 0.4 K, with most uncertainties under 0.15 K. Given that we use the MCMC electronic boresight algorithm when testing our lunar calibration method, we expect the simulated antenna temperature uncertainties in other months to have a similar simulated antenna temperature uncertainty distribution.

Uncertainty in Pathfinder Lunar Temperature Estimate Similar to the previous section, we propagate $\mathrm{d}\beta$ to find its contribution to Pathfinder's lunar temperature uncertainty. To do so, we first restate Equation 3.22 and replace R with its definition in Section 3.3. Therefore, Pathfinder's lunar temperature is defined as

$$T_{moon} = \frac{T_A - T_{ds}}{\exp[-\beta^2/(2\sigma^2)] \cdot f} \tag{3.31}$$

where T_A is the peak Pathfinder measured antenna temperature from MCMC fitting, and β is the minimum Pathfinder electronic boresight from MCMC fitting. We can then define $\frac{\mathrm{d}T_{moon}}{\mathrm{d}\beta}$ as

$$\frac{\mathrm{d}T_{moon}}{\mathrm{d}\beta} = \frac{T_A - T_{ds}}{f} \cdot \exp(\frac{\beta^2}{2\sigma^2}) \tag{3.32}$$

Given that we are calculating uncertainty during lunar intrusions, we expect $T_A > T_{ds}$ as the Moon will be in the antenna FOV. Therefore, $\frac{\mathrm{d}T_{moon}}{\mathrm{d}\beta}$ is unsigned. We can set the electronic boresight contribution to the lunar temperature uncertainty (which we denote as $\epsilon_{\beta,Moon}$) as

$$\epsilon_{\beta,Moon} = |\mathrm{d}T_{moon}| = \frac{T_A - T_{ds}}{f} \cdot \exp(\frac{\beta^2}{2\sigma^2}) \cdot \mathrm{d}\beta \tag{3.33}$$

Using Equation 3.33, we propagate the MCMC electronic boresight uncertainty for lunar intrusions in October 2021. The distribution of these uncertainties are displayed in Figure 3-21.

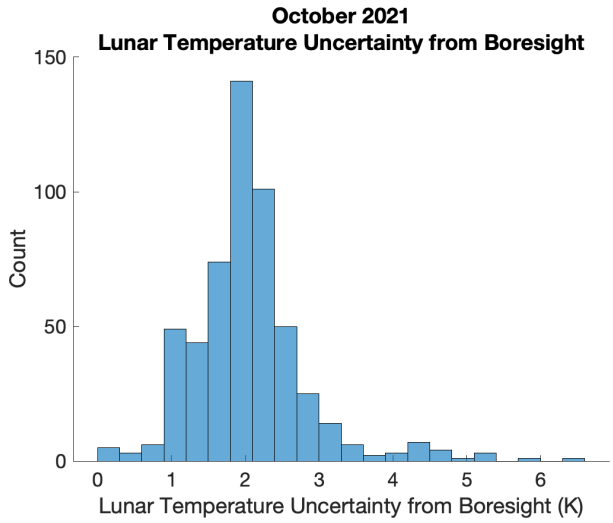

Figure 3-21: The contribution of MCMC electronic boresight uncertainty to the October 2021 Pathfinder lunar temperature uncertainties as calculated using Equation 3.33. All channels' results are displayed in this histogram.

Figure 3-21 shows that the electronic boresight estimate may contribute up to 7 K of uncertainty to the Pathfinder lunar temperature estimate, with most uncertainties being less than 3 K. The uncertainties here are larger than those in Figure 3-20 because we divide by both the antenna response R and the solid angle ratio f in Equation 3.33. When performing our lunar calibration method on other months, we expect the electronic boresight's contribution to lunar temperature uncertainty to have a similar distribution.

3.12 Summary

In Chapter 3, we outline the data preparation strategy to use TROPICS lunar observations for lunar calibration. We continue the data quality analysis presented in Chapter 2, giving particular focus in how Pathfinder's pointing errors can be accounted for. After data preparation, we continue to the lunar calibration procedure and compare the prepared TROPICS observations to simulation in Chapter 4.

This page is intentionally left blank.

Chapter 4

Lunar Intrusion Calibration Analysis

After preparing the Pathfinder lunar observation data, we compare the estimated lunar temperatures to the simulated ones from Yang and Burgdorf's lunar model. This chapter outlines the filtering procedure for lunar intrusions as well as the lunar calibration results.

4.1 Filtering Procedure

Due to data availability, we use Pathfinder's lunar observations from October 2021 to December 2021. Data from October 2021, as mentioned in Section 3.4, is used to calculate angle offsets to try to determine Pathfinder's pointing error. We evaluate the performance of the lunar calibration using lunar intrusions in November and December 2021.

Not all lunar intrusions are usable for calibration, though. Sometimes, the Moon barely appears in the antenna FOV, leading to low lunar intrusion temperatures that are hard separate from the deep space measurements. In addition, lunar intrusions with very few Pathfinder measurements are difficult to fit because the MCMC algorithm performs better with more points. We filter for lunar intrusions that (1) have large, discernible temperature signals, (2) have close MCMC fits for both measured antenna temperature and electronic boresight, and (3) have the Moon sufficiently in the antenna FOV. To satisfy these requirements, we outline the filtering requirements

that all lunar intrusions must satisfy in order to be used in lunar calibration. These requirements are listed in Table 4.1.

Table 4.1: The data filtering conditions that all lunar intrusions must pass to be used for lunar intrusion calibration

Filter	**Reasoning**	**Reference Section**
$\sigma_{ds,max} > 1$ K	The standard deviation in measured antenna temperature must spike to at least 1 K. This condition is used to detect if there is a usable lunar intrusion signal.	3.2.1
MCMC Electronic Boresight RMSE $< 0.2°$	The MCMC electronic boresight fitting must match the resampled and smoothed input boresight values closely	3.7, 3.8
MCMC Antenna Temperature RMSE < 1 K	The MCMC antenna temperature fitting must closely match the resampled and smoothed input temperature values	3.7, 3.8
All MCMC B must lie within the lunar intrusion time period	The peak measured antenna temperature and minimum β must occur within the detected lunar intrusion time bounds	3.7, 3.8
$\beta_{min,MCMC} < \frac{BW-\phi_M}{2} - \mathrm{d}\beta$	The entire lunar disk must be in the antenna FOV for all β ranges within $\pm\mathrm{d}\beta$ of the minimum MCMC estimate $\beta_{min,MCMC}$	3.11
Number of resampled and smoothed points used in MCMC > 50	Empirical threshold to ensure that the MCMC algorithm has enough samples for reliable fitting	3.7, 3.8

4.2 Results

Using the data filtering from Section 4.1, we run the lunar calibration method on November and December 2021. Figures 4-1 through 4-4 display Channel 1 and Channel 10 results when comparing both lunar temperature and antenna temperature to simulated values for both months. We display Channel 1 and 10's results as they are representative of all channels' performance.

As shown in Figures 4-1 through 4-4, the antenna temperature differences are within 1 K for Channel 1 and 2 K for Channel 10. The equivalent lunar temperature differences, however, are large. The larger differences are likely because we divide by the antenna response R and solid angle ratio f, both of which are at most 1. Other contributors to these differences include our approximation of a circularly symmetric antenna beam pattern instead of accounting for antenna asymmetry and antenna sidelobe sensitivities. In addition, we consider 3 additional sources of error that may contribute to the large lunar temperature differences. We outline how these sources of error can affect our lunar calibration results in Section 4.3.

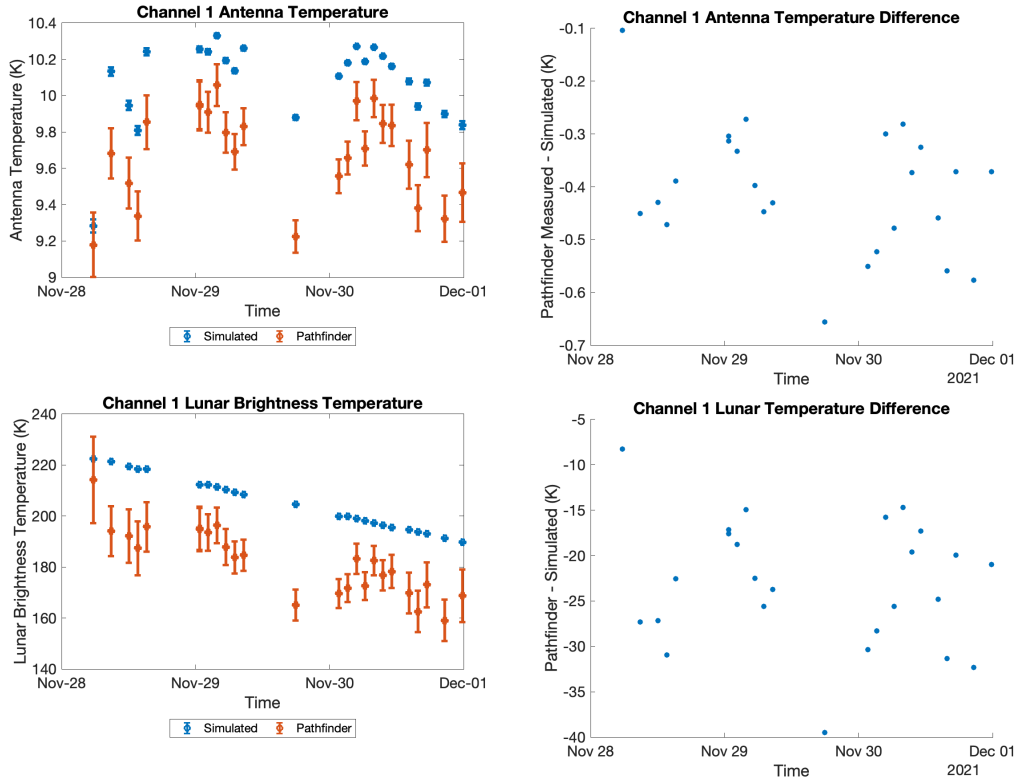

Figure 4-1: The lunar calibration results for Channel 1 lunar intrusions in November 2021. The left column displays the comparison between the Pathfinder temperatures and the simulated values as calculated in Sections 3.8 - 3.10. These simulated values use Yang and Burgdorf's RTM that is tuned to tuned to ATMS observations. The right column displays the difference (Pathfinder - simulated) of the central estimates. Error bars use the uncertainty values calculated in Section 3.11.

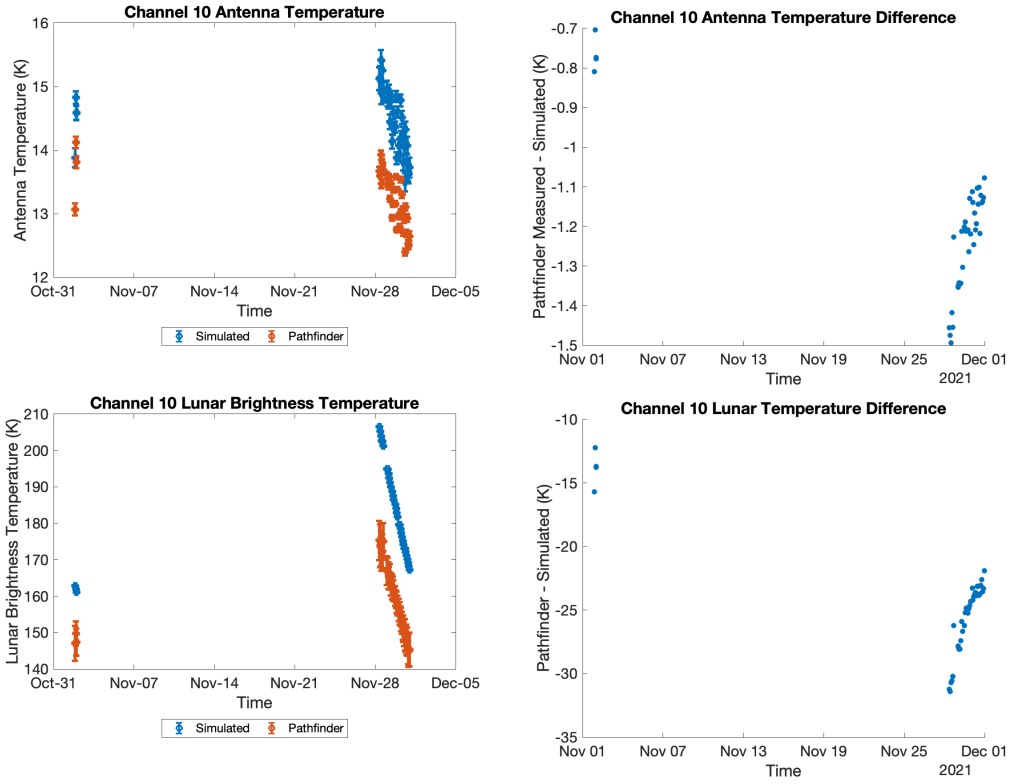

Figure 4-2: The lunar calibration results for Channel 10 lunar intrusions in November 2021. The left column displays the temperature comparison between Pathfinder and simulated temperatures as calculated in Sections 3.8 - 3.10, wher ethe simulated temperatures are calculated using the ATMS-tuned RTM developed by Yang and Burgdorf. Uncertainty values are calculated using Section 3.11. The right column displays the differences (Pathfinder - simulated) of the central estimates.

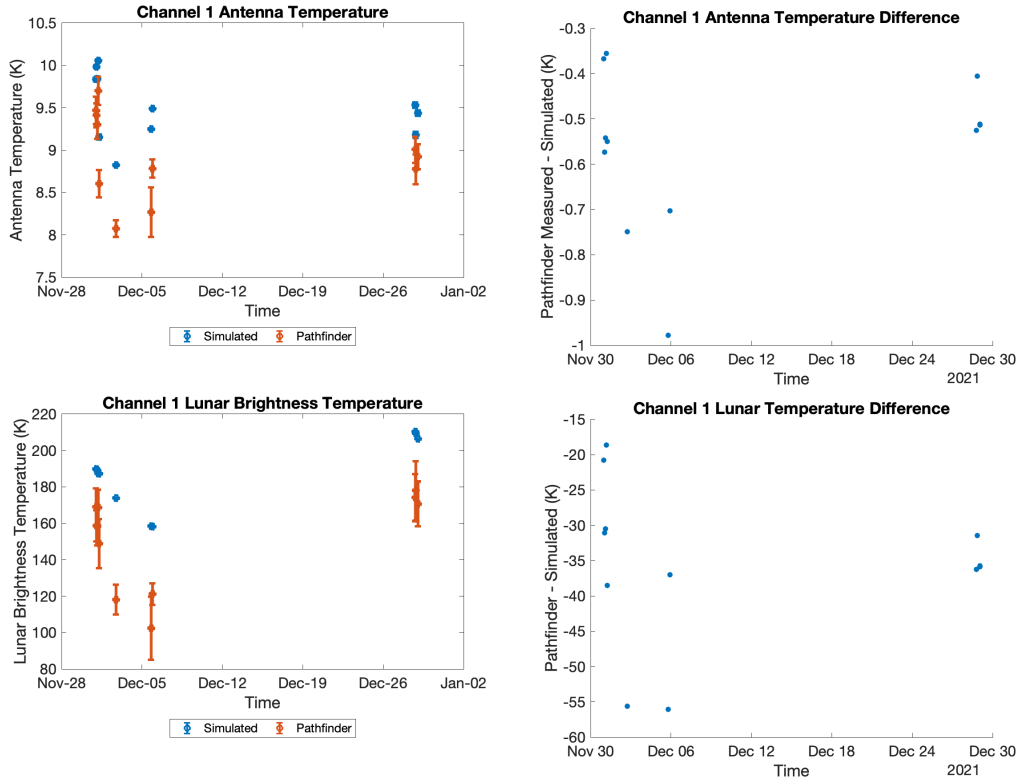

Figure 4-3: Lunar calibration results for Channel 1 lunar intrusions in December 2021. The left column compares Pathfinder's lunar temperature estimates and measured antenna temperatures to those from simulation using Sections 3.8 and 3.10. The simulated temperatures use the ATMS-tuned RTM developed by Yang and Burgdorf. The error bars use the uncertainties calculated from Section 3.11. The right column displays the difference in these temperatures (Pathfinder - simulated).

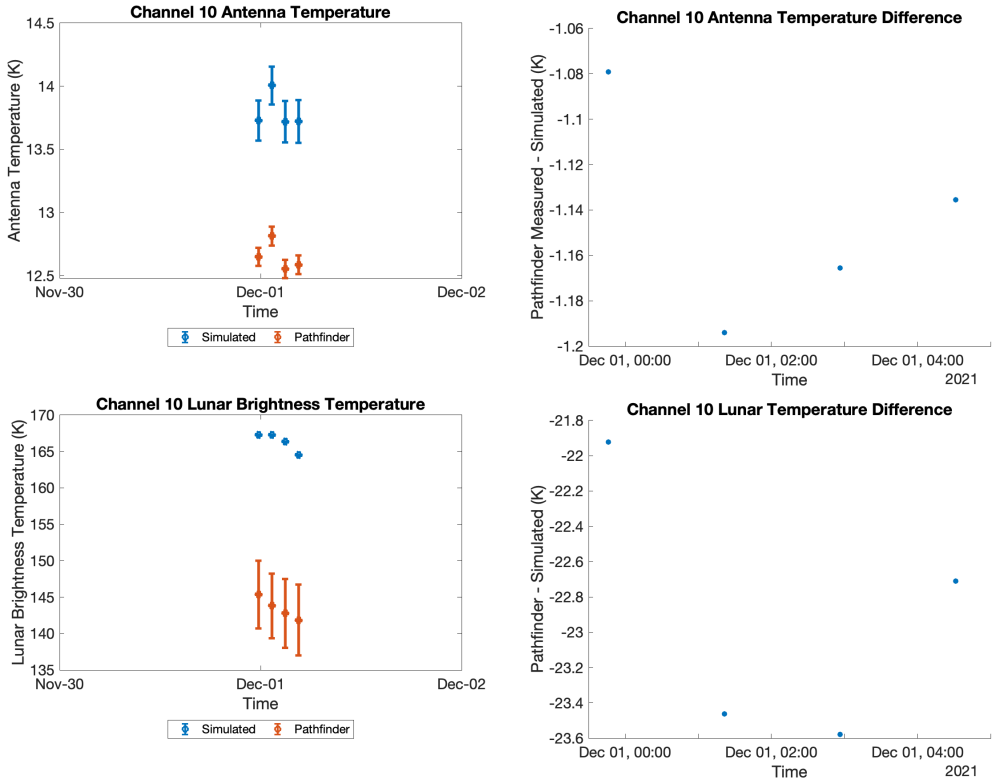

Figure 4-4: Lunar calibration results for Channel 10 lunar intrusions in December 2021. The left column compares Pathfinder's lunar temperature estimate and measured antenna temperature to their simulated counterparts as calculated in Sections 3.8 and 3.10. The simulated values use the ATMS-tuned RTM developed by Yang and Burgdorf. The error bars display the uncertainties calculated in Section 3.11. The right column displays the difference (Pathfinder - simulated) in the central estimates from the right column.

4.2.1 Data Availability Tradeoffs

Another noticeable feature in Figures 4-1 through 4-4 is that the lunar calibration results are only shown for a small portion of each month. For instance, Figure 4-1 only displays dates between November 28th through the 30th, and Figure 4-2 only has usable lunar intrusions in November 1st and the end of November. Likewise, the December lunar calibration results are only valid for the very beginning and end of the month. This gap in lunar calibration is due to two factors: (1) the orbital geometry and (2) the data filtering process outlined in Section 4.1.

Although we cannot control when the Moon falls into the antenna FOV, we can control our data filtering requirements. Our data filtering requirements gauge the performance of the MCMC fitting and the strength of the lunar intrusion signal. Relaxing our filtering requirements in Table 4.1 would yield more lunar intrusions for calibration, but would result in more noisy (and larger) lunar and antenna temperature differences that would later make calibration drift detection more difficult. However, too strict of data filtering requirements will filter out more (if not all) lunar intrusions. As an example, our data filtering for Figure 4-4 only kept four Channel 10 lunar intrusions for December 2021. This phenomenon also extends to the rest of the G-band (Channels 9-12). While the G band may yield fewer lunar intrusions that satisfy the data filtering requirements, the results that do pass may be more reliable than the W/F band's results. This trend occurs because the G band has a higher SNR and typically has more pronounced lunar intrusion signals due to the smaller beamwidths. A study could be done as future work to further investigate the tradeoffs between the data filtering and lunar calibration results to refine the data filtering requirements.

4.2.2 Lunar Calibration Error Bounds

In addition to analyzing lunar calibration results, we also characterize the lunar calibration error by comparing the results to two alternative situations:

1. The Moon lies in the center of the antenna FOV, so $\beta = 0^\circ$ and $R = 0$, or
2. The Moon lies on the edge of the antenna FOV, so $\beta = (BW/2)^\circ$ and $R = 0.5$, where BW is the mean antenna beamwidth as stated in Table 3.1.

For notation purposes, we name (1) to be the Center situation and (2) to be the Edge situation. Figure 3-18 shows how these cases compare to the MCMC estimated β.

Besides the changes in β, we assume all other factors such as the antenna beam pattern and the solid angle ratio f remain the same. By comparing our lunar calibration results to these situations, we attempt to bound the lunar calibration error (assuming no model issues) and characterize lunar calibration performance. Figure 4-6 displays the bounds for the lunar calibration error when comparing lunar temperature estimates and antenna temperatures.

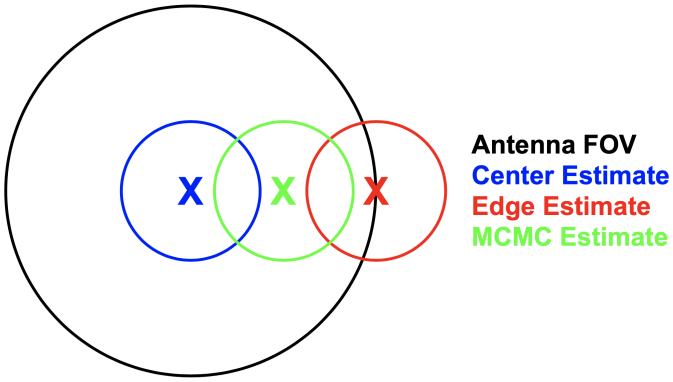

Figure 4-5: A visualization of how the Center and Edge cases compare to the MCMC estimate. The antenna FOV is defined by the mean FWHM beamwidth BW such that the antenna response R is a highest at its center (effectively, we assume a circularly symmetric antenna beam). The "X" symbols indicate the center of the Moon for each given estimate, and the smaller circle of the same color is the corresponding location of the lunar disk. The Center case's "X" lies in the center of the antenna FOV because $\beta = 0°$, and the Edge case's "X" lies at the edge of the antenna FOV as $\beta = (BW/2)°$. The MCMC estimate's electronic boresight is $\beta \in [0, BW/2]°$, so its estimate for lunar position lies between those of the Center and Edge estimates. As a note, all β are unsigned, so this visualization is rotationally symmetric.

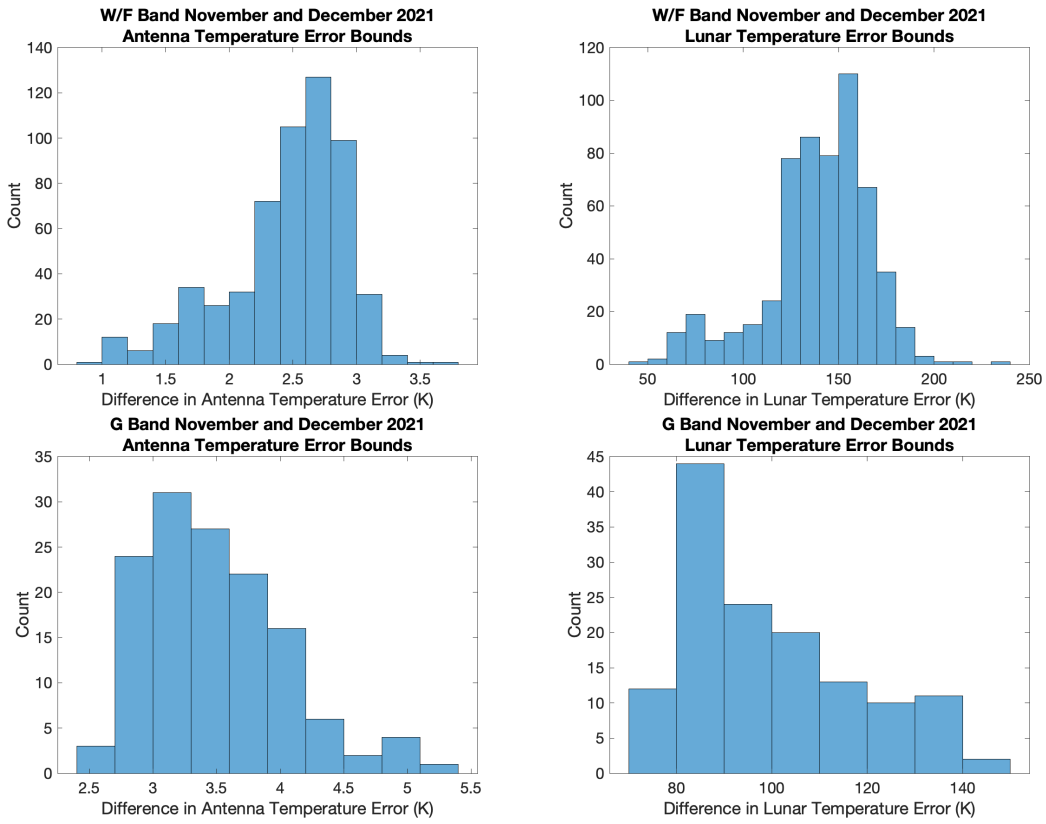

Figure 4-6: The overall error bounds for lunar calibration when comparing lunar temperature estimates (left column) and antenna temperature estimates (right column) for lunar intrusions in November and December 2021 for the W/F band (Channels 1-8, in the top row) and the G band (Channels 9-12, in the bottom row). The error bounds are the maximum magnitude of change in lunar calibration error between the assumptions $\beta = 0°$ and $\beta = (BW/2)°$.

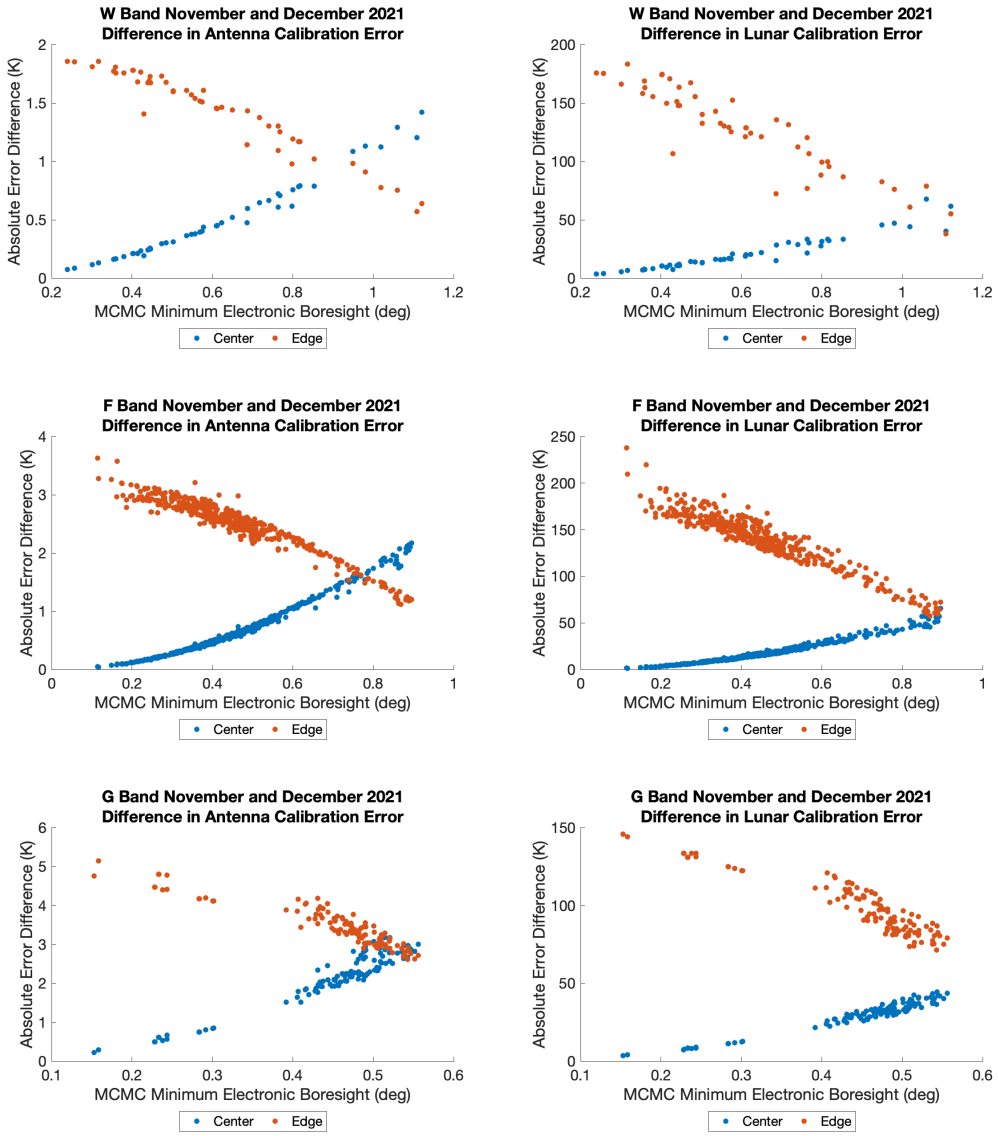

Figure 4-7: The relationship between the absolute change in lunar calibration error (or absolute error difference) for antenna temperature (left) and lunar temperature (right) for the W band (Channel 1), the F band (Channels 2-8), and the G band (Channels 9-12) for $\beta = 0°$ (Center) and $\beta = BW/2°$ (Edge). We separate the W and F bands to more easily display the relationship's behavior over varying β.

Figure 4-6 shows that the W/F band's lunar calibration error may vary up to 4 K and 250 K when comparing antenna and lunar temperatures, respectively. Similarly, the G band's lunar calibration error may vary up to 5.5 K and 150 K for antenna and lunar temperatures, respectively. The large error bounds in lunar temperature calibration error for all bands further demonstrate that using antenna temperatures is more feasible for lunar calibration. The large lunar temperature differences are likely due to the same sensitivities as described in Section 4.2.

In addition to displaying the histogram of error bounds in Figure 4-6, we analyze the relationship between the error bounds and the minimum electronic boresight estimated by MCMC fitting.

Figure 4-7 shows that the absolute calibration error varies with our estimated electronic boresight, with smaller β having larger error bounds. For small β, the W band's (Channel 1) calibration error for antenna temperature can vary by as much as 2 K, while for the G band, the antenna temperature calibration error may vary by 5 K. The variation in absolute error difference is due to antenna beamwidth. As the G band has the smallest antenna beamwidths, the Moon occupies more of the antenna FOV than when in the W/F band antenna's FOV. The position of the Moon in the antenna FOV has a larger influence on simulated temperature and lunar temperature estimates.

In addition, Figure 4-7 shows that the difference in calibration error when assuming $\beta = 0°$ and $\beta = BW/2°$ are mirrored. If our estimated β is small, then the TROPICS Pathfinder measured temperature is high as the Moon is close to the center of the antenna beam. Therefore, if we assume $\beta = 0°$, then the Pathfinder lunar temperature estimate and the corresponding simulate antenna temperature will change very little. This behavior can be seen in Figure 4-7; as β decreases, the absolute calibration error difference for the Center situation approaches 0 K. On the other hand, the absolute calibration error for the Edge situation is much higher when $\beta \to 0°$. As we assume $\beta = BW/2°$ in the Edge situation, the large change in β leads us to overestimate Pathfinder's lunar temperature and underestimate the corresponding simulated lunar temperature. Therefore, as $\beta \to 0°$, the absolute error difference

from the Edge situation increases.

From Figures 4-6 and 4-7, we find that the error bounds are highest when our MCMC estimated β is low and lowest at high MCMC estimated β. However, the error bounds for all bands are quite high. The maximum antenna temperature error bounds are approximately 2 K, 4 K, and 5 K for the W, F, and G bands, respectively. The antenna temperature error bounds increase as the antenna beamwith decreases because small fluctuations in β will yield a larger change in antenna response. Given that the antenna temperature differences displayed in Figures 4-1 through 4-4 range from ± 2 K, the lunar calibration results can vary. Although Figures 4-1 through 4-4 show low antenna temperature differences, this variation may make it difficult to detect calibration drift using TROPICS antenna temperatures. Without consistent antenna temperature differences and low error bounds, it is difficult to pinpoint whether changes in antenna temperature difference are due to calibration drift, the three sources of error as outlined in Section 4.3, or other sources. Addressing these sources of error can potentially decrease the error bounds and also the antenna temperature differences to make TROPICS more usable for lunar calibration.

4.3 Sources of Error

In order to perform accurate and reliable lunar calibration, we expect that the antenna temperature and lunar temperature differences are consistent over time so that small changes in these temperature differences can be attributed to calibration drift. However, as mentioned in Section 4.2, both the antenna and lunar temperature differences fluctuate. We consider 3 possible sources of error in this section and in Future Work (Section 5.1) that can contribute to the fluctuations in antenna and lunar temperature differences as well as the error bounds:

1. TROPICS data,
2. Yang and Burgdorf's lunar RTM from [21], and
3. Lunar calibration model method.

In this section, we outline how each source of error can affect lunar calibration results and add other comments in Future Work (Section 5.1).

4.3.1 TROPICS Data

One source of error in the lunar calibration model is the TROPICS dataset, primarily two aspects: (1) Calibration, and (2) Pointing. For (1), the calibration of TROPICS data is still in progress. There can possibly be other calibration errors besides calibration drift that can affect the antenna and lunar temperature differences and error bounds in Figure 4-1 through 4-7. We expect that the main calibration procedure will be adjusted and finalized with more data and TROPICS satellites in the future. Future work can rerun this lunar calibration procedure with newer versions of the TROPICS dataset to reassess performance.

Regarding (2), the TROPICS Pathfinder dataset provides unsigned values for the electronic boresight β. We therefore do not have directional information about β, so we do not know where the Moon is located in the antenna FOV. To account for this fact, we approximate the antenna beamwidth as the mean of the CT and AT beamwidths as stated in Section 3.3, effectively approximating the antenna FOV footprint as a circle rather than an ellipse. Our values for R, then, will be different than what the antenna response would be without this approximation. Given that the lunar temperature differences involve a division by R, small changes in R can affect Pathfinder's lunar temperature estimate. Although the antenna temperature comparison also involves R, the results are less sensitive to R because we calculate antenna temperature by *multiplying* by R rather than dividing. To further analyze this source of error, we explore how changes in β (and therefore R) can affect the lunar calibration error in Section 4.2.2. Although β remains unsigned, bounding the lunar calibration error will help us characterize the performance of this calibration method.

4.3.2 Lunar RTM

Yang and Burgdorf's RTM can also be a potential source of error in this lunar calibration because the model is tuned to ATMS observations [21]. They calculate the effective lunar emissivities for ATMS channels and fit an exponential function to calculate the effective lunar emissivities for any other frequency [21].

In this work, we assume that this exponential function holds true for TROPICS frequencies, despite, as noted in Table 1.4, the frequency matchups between the TROPICS channels and those used by Yang and Burgdorf for either RTM calibration or validation. If the effective lunar emissivity for the TROPICS frequencies are different than predicted from this exponential curve, then the simulated lunar brightness temperature outputted from Yang and Burgdorf's RTM will also change and therefore affect the lunar calibration results.

In addition, the frequency matchups between TROPICS Pathfinder and Yang and Burgdorf's RTM are also subject to variation due to each channel frequency's bandwidth as noted in Table 1.4. In this work, we assume each channel frequency stays at the constant central frequency value. Future work can further investigate the effect of the bandwidth on lunar calibration results.

4.3.3 Lunar Calibration Methodology

The overall lunar calibration methodology outlined in this thesis may need to be adjusted as well. In order to investigate whether adjustments are necessary, future work can perform the lunar calibration procedure but replace the TROPICS dataset with ATMS observations. By performing this replacement, we eliminate the 2 previous sources of error described in Sections 4.3.1 and 4.3.2 because Yang and Burgdorf's RTM is tuned to ATMS data, and the ATMS dataset is much larger than the TROPICS dataset with a documented calibration procedure.

Ideally, we thus expect the ATMS lunar calibration results using this lunar calibration framework to be more precise than when using the TROPICS dataset. Higher precision would translate to more consistent antenna and lunar temperature differ-

ences as well as lower error bounds as calculated in Section 3.4. If this behavior does not occur, then the lunar calibration methodology may need to be adjusted.

4.4 Summary

In this chapter, we outline our data filtering criteria and also compare the Pathfinder lunar temperature estimate and measured antenna temperatures to Yang and Burgdorf's simulation as calculated in Chapter 3. From our November and December 2021 results, we find that comparing antenna temperatures is more feasible for calibration drift detection than lunar temperatures because the antenna temperature differences are smaller than the lunar temperature differences and are also less sensitive to pointing error. However, our results demonstrate that the lunar calibration error for antenna temperature may vary up to 4 K for the W/F bands and 5.5 K for the G band. These error bounds indicate that the reliability of said lunar calibration results need more refinement. We outline three possible sources of error and how they can affect the results. In Chapter 5, we outline avenues of future work that can potentially improve the lunar calibration results and reliability.

This page is intentionally left blank.

Chapter 5

Conclusion

In this thesis, we evaluate the use of TROPICS Pathfinder lunar observations for lunar calibration. To do so, we create a framework for lunar calibration that includes detecting lunar intrusions by analyzing Pathfinder's measured antenna temperatures, evaluating Pathfinder data quality, accounting for pointing error, and estimating the lunar temperature estimate using MCMC. After preparing the TROPICS Pathfinder lunar observations, we compare the measurements in November and December 2021 to Yang and Burgdorf's lunar RTM using two avenues: lunar brightness temperature comparison and antenna temperature comparison. Overall, the prepared TROPICS Pathfinder lunar observations differed from the RTM with a mean of 25.94 K for lunar brightness temperature and 0.68 K for antenna temperature. We show that it is more feasible to use TROPICS Pathfinder lunar observations for lunar calibration when comparing antenna temperatures rather than lunar temperatures. However, the antenna temperature differences may fluctuate as much as $\pm$2K, $\pm$4K, and $\pm$5K for the W, F, and G bands, respectively. Although the antenna temperature differences are low, the current error bounds needs more lunar model offset work. We outline possible sources of error and recommend that future work investigate and address each source to improve lunar calibration results and reliability. Overall, we show that the lunar temperature model needs more work to match the TROPICS data. There are offsets between the TROPICS Pathfinder observations and Yang and Burgdorf's simulation, but the common trends appear promising.

5.1 Future Work

The work in this thesis can be extended to improve the reliability of the lunar calibration. In this section, we outline multiple avenues of future work.

5.1.1 Encoder Angle Error Characterization

In Section 3.4.1, we discuss the potential effects that the encoder angle jitter can have on pointing and lunar intrusion. In particular, Figure 3-9 demonstrates that the encoder angle has a beating pattern similar to an undersampled sinusoid. This behavior is likely due to the fact that the encoder wheel controller is oscillating around the desired encoder angle value. Characterizing this beating pattern would be useful in estimating and potentially correcting for the encoder angle jitter. In addition, new software for the encoder wheel controller can also lessen the jitter.

5.1.2 Incorporating Direction into Lunar Calibration

As mentioned in Section 4.2, having information of where the Moon is in the antenna FOV rather than the unsigned electronic boresight would be helpful for the lunar calibration results. Provided that this information is available, we would no longer need to approximate the antenna FOV footprint as a circle and can instead use both the CT and AT antenna beamwidths in our calculations. In particular, we can calculate R as a function of 3-dimensional Gaussian function rather than a 2-dimensional one as detailed in Equation 3.9. Using the updated antenna response values may improve lunar calibration results, particularly when calculating Pathfinder's lunar temperature estimate and the simulated antenna temperature.

5.1.3 Antenna Pattern and Sidelobe Sensitivity Analysis

As mentioned in Section 3.4, the relationship between the electronic boresight β and the measured antenna temperature is vague for low β, which is when the satellite expects the Moon to be in the antenna FOV. As β decreases, we expect the measured

antenna temperature to increase. However, the TROPICS Pathfinder measurements do not consistently follow this behavior. In this thesis, we assume that this vague relationship is due to angle offsets in β. There can be additional causes such as antenna pattern and sidelobe sensitivities. Future work can analyze these sensitivies and their potential effect on lunar calibration.

5.1.4 Adjustments to Yang and Burgdorf's RTM

We can make adjustments to Yang and Burgdorf's RTM that can potentially decrease the lunar temperature and antenna temperature offsets that are shown in Figures 4-1 through 4-4, respectively. Having lower differences between Pathfinder's lunar observations and this RTM would make long term calibration drift detection easier.

One such adjustment is to tune Yang and Burgdorf's RTM to TROPICS observations. As mentioned in Chapter 1.3.2, Yang and Burgdorf's RTM first calculate the lunar blackbody emissions given lunar phase and frequency [21]. They then calibrate this model by comparing these blackbody emissions to ATMS Full Moon observations and estimating the lunar emissions. A possible extension is to perform a similar RTM tuning using TROPICS lunar observations for all TROPICS frequencies so that all TROPICS Pathfinder channels have frequency and beamwidth matches in the RTM. In this thesis, we assumed that the RTM calibrated on ATMS observations would be close enough for TROPICS Pathfinder lunar calibrations.

Another adjustment would be to filter Pathfinder's lunar observations based on the Moon's path in the antenna FOV. In Section 1.3.2, we also mention that Yang and Burgdorf validate their RTM by comparing the modeled lunar brightness temperatures to lunar observations from multiple NOAA spacecraft. All lunar observations used in this validation had the Moon pass through the center of the antenna FOV [21]. Because the electronic boresight angles provided in the TROPICS Pathfinder dataset (as mentioned in Section 2.2) are unsigned, we do not have the directional information needed to filter for lunar observations that are in the center of the antenna FOV. If this information is provided in the future, we can filter TROPICS lunar observations and rerun lunar calibration.

5.1.5 Adjusting the Lunar Calibration Model

As outlined in Section 4.3, one source of error is the lunar calibration methodology outlined in this work. In order to determine whether adjustments need to be made in this work, future work can run the lunar calibration method using ATMS lunar observations rather than TROPICS Pathfinder observations. Given that Yang and Burgdorf's RTM is tuned to ATMS observations and that ATMS has more finalized calibration, we expect the lunar calibration results to be more precise and reliable than when using the TROPICS dataset. If this behavior does not occur, then the lunar calibration model likely needs adjustments.

5.1.6 Detecting Calibration Drift

After comparing TROPICS lunar observations to simulation, the next step is to detect and correct for calibration drifts. As Figures 4-1 through 4-4 display, there are often "clumps" of lunar calibration results that cluster around similar error values. There are two main contributions to said errors: (1) the error from the lunar calibration model outlined in this work, and (2) Pathfinder's calibration drift. One way to estimate calibration drift would be to find the mean of each of the lunar calibration "clumps" and assume that the "noise" in the clumps are attributed to (1). By doing so, though, a time window needs to be defined to define the boundaries of these error clumps if multiple are close together temporally. Future work can perform statistical analysis to differentiate between errors from (1) and (2), and also estimate the calibration drift over time.

5.1.7 Performing Lunar Calibration for a Longer Time Frame

In this thesis, we calculate our angle offsets using October 2021 TROPICS Pathfinder lunar observations in Section 3.4 and then test our lunar calibration method on Pathfinder data in November and December 2021. Ideally, lunar calibration should be performed over more months (or, perhaps, years) to detect long-term calibration drifts. Therefore, future work will include running this lunar calibration scheme over

a longer time frame and determining how well the angle offsets (that use October 2021 observations) perform for later datasets. In this way, we can also determine how often angle offset recalculation as done in Section 3.4 needs to be performed (if any).

5.1.8 Incorporating Solar Intrusions

In this thesis, we focus solely on lunar intrusions. However, another possible vicarious calibration source is the Sun. The Sun has a higher temperature than the Moon, so solar intrusions would not only be easier to detect but would also have lower SNR.

Currently, though, there are no radiative transfer models for the Sun in microwave frequencies. In addition, the Sun is highly seasonal; solar temperatures can vary widely because of factors such as sun spots and long-term solar cycles [15]. If this behavior can be accurately and reliably modeled, we can use both lunar and solar intrusions in calibration. With more vicarious calibration targets, we can more frequently monitor Pathfinder's calibration performance.

5.1.9 Performing Lunar Calibration on the TROPICS Constellation

As the TROPICS constellation has yet to be launched successfully, we use Pathfinder data for lunar calibration. Once the constellation is in operation, we can perform an identical lunar calibration procedure for each satellite. This procedure would include spacecraft-specific characterizations related to pointing.

This page is intentionally left blank.

Appendix A

Main Notation and Equations for Lunar Calibration

Table A.1: Main Mathematical Symbols in Lunar Calibration

Symbol	**Meaning**	**Units**
β	Electronic Boresight	deg
β_{sim}	Simulated Electronic Boresight	deg
G	Gain	K / DN
DN	Digital Count	unitless
T_A	Antenna Temperature	K
T_{ds}	Deep Space Temperature	K
T_{moon}	Lunar Brightness Temperature	K
$T_{moon,sim}$	Simulated Lunar Brightness Temperature from [21]	K
ϕ_M	Angle Subtended by Moon	deg
Ω_A	Antenna Solid Angle	sr
Ω_M	Lunar Solid Angle	sr
η_{ML}	Antenna Main Beam Efficiency	%
f	Solid Angle Ratio	unitless
R	Normalized Antenna Response	unitless
θ_M	Lunar Phase Angle	deg
BW	Mean Full-Width Half Max Antenna Beamwidth	deg

Table A.2: Main Equations used in Lunar Calibration

Equation	**Description**
$T_A = T_{ds} + R * f * T_{moon}$	General Antenna Temperature Model
$\sigma = \frac{0.5BW}{\sqrt{2\ln 2}}$	Standard Deviation of Antenna Response Model
$R = \exp(-\frac{\beta^2}{2\sigma^2})$	Antenna Response Formula
$F_{nML}(\theta, \phi) = e^{-\ln(2)(2\theta/BW)^2}$	Gaussian Model of Antenna Main Beam
$\Omega_M = \int_0^{2\pi} \int_0^{\phi_M/2} F_{nML}(\theta, \phi) \sin\theta d\theta d\phi$	Lunar Solid Angle Equation
$\Omega_A = \frac{1}{\eta_{ML}} \int_0^{2\pi} \int_0^{2\pi} F_{nML}(\theta, \phi) d\Omega$	Antenna Solid Angle Equation
$f = \frac{\Omega_M}{\Omega_A}$	Solid Angle Ratio

Appendix B

Pathfinder Antenna Line of Sight Calculations

This section describes the Pathfinder antenna line of sight (LoS) calculations, particularly the role of the encoder angle. Before calculating the line of sight vectors, we define four coordinate systems from [18]:

- The Payload Coordinate System (PCS),
- The Payload Alignment Coordinate System (PACS),
- The Attitude Determination and Control System (ADCS) Body Coordinate System (BCS), and
- The Earth-Centered, Earth-Fixed Frame (ECEF).

The LoS are initially defined in PCS, but must be converted to ECEF in order to calculate the electronic boresight. To do this procedure, TROPICS preprocessing in [18] performs the following conversions:

$$PCS \rightarrow PACS \rightarrow BCS \rightarrow ECEF \tag{B.1}$$

A visualization of said coordinate system conversions and the coordinate systems themselves are shown in Figure B-1. We first define the nominal boresight unit vector

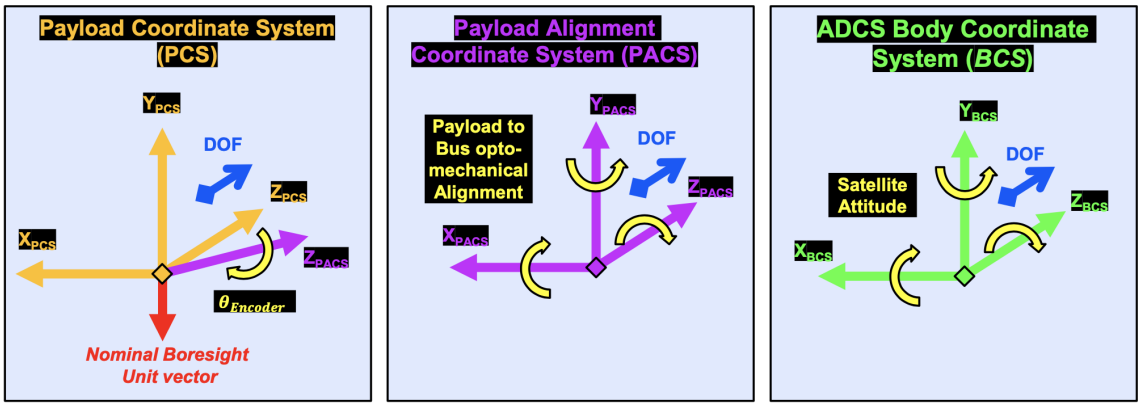

Figure B-1: The coordinate systems defined in [18] along with the transformations from PCS to BCS (left to right). DOF stands for direction of flight. The yellow arrows describe the transformations required to convert to the coordinate system to the right of the one they are displayed in. For BCS, the yellow arrows display the conversion to ECEF.

(also known as the LoS) in PCS as

$$\begin{bmatrix} 0 & -1 & 0 \end{bmatrix}^T \tag{B.2}$$

We can therefore perform the first conversion from PCS to PACS by rotating the LoS by the encoder angle $\theta_{encoder}$ using the quaternion

$$q_1 = \begin{bmatrix} q_s \\ q_x \\ q_y \\ q_z \end{bmatrix} = \begin{bmatrix} \cos\frac{-\theta_{encoder}}{2} \\ \left\|\overrightarrow{Z_{PACS}}\right\| \sin\frac{-\theta_{encoder}}{2} \end{bmatrix} \tag{B.3}$$

where $\overrightarrow{Z_{PACS}}$ accounts scan axis misalignment and is determined by payload mechanical inspections [18]. In Equation B.3, $\left\|\overrightarrow{Z_{PACS}}\right\|$ is the element-wise absolute value of $\overrightarrow{Z_{PACS}}$. Thus, q_1 accounts for scan axis alignment as well as the encoder angle.

After converting the LoS from PCS to PACS, we convert to BCS by rotating the vector by the spacecraft-specific direction cosine matrices (DCM) that are determined by opto-mechanical alignment data. We refer to this DCM as $\mathcal{A}_{PACS2BCS}$. After this conversion, we rotate from BCS to ECEF using a quaternion that incorporates

satellite attitude data. We refer to this quaternion as q_3.

From these quaternions and $\mathcal{A}_{PACS2BCS}$, we consolidate the coordinate conversion to

$$q_2 = \texttt{dcm2quat}(\mathcal{A}_{PACS2BCS}) \tag{B.4}$$

$$q_{All} = (q_1 * q_2) * q_3 \tag{B.5}$$

$$\mathcal{B}_{PCS2ECEF} = \texttt{quat2dcm}(q_{All}) \tag{B.6}$$

where `dcm2quat` refers to the conversion from a DCM to a quaternion, and `quat2dcm` refers to the opposite conversion. Given the LoS in PCS (denoted as LoS_{PCS}), we can find LoS_{ECEF} by calculating

$$LoS_{ECEF} = \mathcal{B}_{PCS2ECEF} * LoS_{PCS} \tag{B.7}$$

where LoS_{ECEF} is the LoS in ECEF. This derived value is used when calculating electronic boresight.

This page is intentionally left blank.

Bibliography

[1] Amsu overview, 2016.

[2] Mhs overview, 2023.

[3] The Almanac. Moon phases calendar, 2023.

[4] William J Blackwell, S Braun, R Bennartz, C Velden, M DeMaria, R Atlas, J Dunion, F Marks, R Rogers, B Annane, et al. An overview of the tropics nasa earth venture mission. *Quarterly Journal of the Royal Meteorological Society*, 144:16–26, 2018.

[5] William J Blackwell and Scott Braun. Mission overview, 2015.

[6] Shannon T. Brown, Shailen Desai, Wenwen Lu, and Alan B. Tanner. On the long-term stability of microwave radiometers using noise diodes for calibration. 2007.

[7] Shannon T. Brown and Christopher S. Ruf. Determination of an amazon hot reference target for the on-orbit calibration of microwave radiometers. *Journal of Atmospheric and Oceanic Technology*, 2005.

[8] Ahmet Cecen. Multivariate polynomial regression, 2023.

[9] Angie Crews, William J. Blackwell, R. Vincent Leslie, Michael Grant, Hu Yang, and Kerri Cahoy. Correcting calibration drifts using solar and lunar intrusions for miniaturized microwave radiometers. *IEEE Transactions on Geoscience and Remote Sensing*, 2021.

[10] David Draper and David Newell. Global precipitation measurement (gpm) microwave imager (gmi) after four years on-orbit. *IEEE*, 2018.

[11] David W. Draper, David A. Newell, Darren S. McKague, and Jeffrey R. Piepmeier. Assessing calibration stability using the global precipitation measurement (gpm) microwave imager (gmi) noise diodes. *IEEE Journal of Selected Topics in Applied Earth Observations and Remote Sensing*, 2015.

[12] David W. Draper, David A. Newell, Dennis A. Teusch, and Peter K. Yoho. Global precipitation measurement microwave imager prelaunch hot load calibration. *IEEE Transactions on Geoscience and Remote Sensing*, 2013.

[13] Masanori Hanada and So Matsuura. *MCMC from Scratch: A Practical Introduction to Markov Chain Monte Carlo*. Springer, 2022.

[14] Paul O. Hayne, Joshua L. Bandfield, Matthew A. Siegler, Ashwin R. Vasavada, Rebecca R. Ghent, Jean-Pierre Williams, Benjamin T. Greenhagen, Oded Aharonson, Catherine M. Elder, Paul G. Lucey, and David A. Paige. Global regolith thermophysical properties of the moon from the diviner lunar radiometer experiment. 2017.

[15] Christian Ho, Stephen Slobin, Anil Kantak, and Sami Asmar. Solar brightness temperature and corresponding antenna noise temperature at microwave frequencies. 2008.

[16] Stephen J. Keihm. Interpretation of the lunar microwave brightness temperature spectrum: Feasibility of orbital heat flow mapping. *Planetary Science Institute, Science Applications*, 1984.

[17] Jet Propulsion Laboratory. Jet propulsion laboratory horizons system, 2023.

[18] R. Vincent Leslie, Mike DiLiberto, and William J Blackwell. Time-resolved observations of precipitation with a constellation of smallsats: Level-1 radiance algorithm theoretical basis document. Technical report, 2022.

[19] National Aeronautics and Space Administration Goddard Earth Science Data Information and Services Center (GES DISC), Goddard, Maryland 20771. *User Guide for TROPICS Data Products*, 2021.

[20] Arne Schroder, Axel Murk, Richard Wylde, Karl Jacob, Kevin Pike, Marc Bergada Pujades, and Ville Kangas. Electromagnetic design of calibration targets for metop-sg microwave instruments. 2017.

[21] Hu Yang and Martin Burgdorf. A calibrated lunar microwave radiative transfer model based on satellite observations. *Remote Sensing*, 2022.

[22] Hu Yang and Fuzhong Weng. Corrections for on-orbit atms lunar contamination. *IEEE Transactions on Geoscience and Remote Sensing*, 2016.

[23] John Xun Yang, Darren S. McKague, and Christopher S. Ruf. Boreal,temperate, and tropical forests as vicarious calibration sites for spaceborne microwave radiometry. 2015.